2012

Density Functional Theory Calculations on Hydrated Dimethylarsinic Acid and Iron Oxide Clusters

Adrian Adamescu
Wilfrid Laurier University, adam5027@mylaurier.ca

Density Functional Theory Calculations on Hydrated Dimethylarsinic Acid and Iron Oxide Clusters

Adrian Adamescu

Honours Bachelor of Mathematics, University of Waterloo, 2005

Honours Bachelor of Science, University of Waterloo, 2008

THESIS

Submitted to the Department of Chemistry

in partial fulfillment of the requirements for

Master of Science

Wilfrid Laurier University

Acknowledgments

I would like to thank my supervisors Dr. Hind Al-Abadleh and Dr. Ian Hamilton for giving me the opportunity to work with them, both as a research assistant and as a Chemistry Master's student. They have both provided me with an excellent example of what it means to be a scientist at a great institution and I really appreciate their help and guidance throughout my educational journey here at Wilfrid Laurier University. Working with them has been a pleasure. In addition I would also like to thank my committee members Dr. Scott Smith and Dr. Shohini Ghose for their advice and valuable input throughout my studies, as well as my external examiner Dr. John Goddard.

Thank you to all the past and current members of our research group who have provided me with helpful input, especially Holly Gray, Julia Tofan, Gregory Wentworth, Marshall Lindner and Derek Arts.

A special thank you to my parents for teaching me the importance of a good education (amongst many other things) and their continuous support, as well as my sister Alina for always being there as a true friend. I would also like to thank God, from whom all blessings come and His son Jesus Christ in whose footsteps I try to walk every day, looking up to His example of love, humility and kindness towards all.

I dedicate this thesis to my beautiful and loving wife Andreea and our daughter Abigail. I have been truly blessed with such an amazing wife who is supportive and kind, as well as an incredibly cute baby girl who brought so much joy to our lives. Andreea, you're my best friend and the love of my life.

List of Publications

1) Adamescu, A.; Hamilton, I.; Al-Abadleh, H.A. Thermodynamics of Dimethylarsinic Acid and Arsenate Interactions with Hydrated Iron-(Oxyhydr)oxide Clusters: DFT Calculations, Environmental Science and Technology, 2011, 45, 10438-10444.

2) Adamescu, A.; Mitchell, W.; Hamilton, I.; Al-Abadleh H.A. Insights into the Surface Complexation of Dimethylarsinic Acid on Iron (oxyhydr)Oxides from ATR-FTIR Studies and Quantum Chemical Calculations, Environmental Science and Technology, 2010, 44(20), 7802-7807.

3) Adamescu, A.; Gray, H.; Stewart, K.; Hamilton, I.; Al-Abadleh H.A. Trends in the frequencies of $\nu(AsO_xH_{x-1})$ [x = 2-4] in selected As(V)-containing compounds investigated using quantum chemical calculations, Canadian Journal of Chemistry, **2010**, 88, 65-77.

Abstract

Dimethylarsinic Acid (DMA) or $(CH_3)_2AsO_2H$ is an important organoarsenical compound detected in arsenic speciation studies of environmental samples and synthesized during pyrolysis of oil shale. DMA was used historically as a herbicide on large agricultural fields and can be detected in the leachates of landfills rich in waste containing arsenic such as glass, alloys, and semiconductors, as well as biologically pre-treated municipal solid waste. Under certain soil conditions DMA can become bio-available and has the potential to be recycled to more toxic inorganic forms of arsenic. Bioavailability of DMA is largely controlled by the extent of its interactions with reactive components in soil. Little is known about these interactions, particularly with iron oxides that have high affinity to arsenic compounds and are ubiquitous components of soil.

In this thesis, density functional theory (DFT) calculations are used to obtain energies, optimal geometries and vibrational frequencies for hydrated DMA-iron oxide clusters. Calculations were performed using Gaussian 09, running on Sharcnet, with the B3LYP and BMK functionals and the 6-31G(d) and 6-311+G(d,p) basis sets. Solvation is simulated by adding explicit water molecules, as well as using the integral equation formalism polarizable continuum model (IEFPCM) and the universal solvation model (SMD).

Various ligand exchange reactions are constructed to investigate the thermodynamics of inner- and outer-sphere complex formation. The Gibbs free energies of adsorption (G_{ads}) for these reactions are calculated and results indicate that both inner- and outer-sphere complex formation is thermodynamically favourable with bidentate complexes being most

favourable. Similarly, the Gibbs free energies of desorption (G_{des}) are calculated for various desorption reactions of DMA due to interactions with phosphate ions and it is determined that desorption favourability of DMA increases in the order of bidentate < monodentate < outer-sphere.

These theoretical studies are used to explain experimental infrared spectral peaks and provide geometrical parameters useful for modeling x-ray absorption data using extended X-ray absorption fine structure (EXAFS) showing DMA-Fe inter-atomic distances to be within 3.3 - 3.4 Å for the bidentate complexes, within 3.4 - 4.9 Å for monodentate complexes and 4.8 - 6.8 Å for outer-sphere complexes.

Table of Contents

List of Figures

List of Figures continued…

List of Tables

1 Introduction

1.1 Interfacial Geochemistry

A *surface* is the bulk terminated boundary of one phase, usually defined by the top one or two atomic layers of that phase. An *interface,* on the other hand, is the physical boundary between two different or two immiscible bulk phases.[1] This is illustrated in Figure 1 below.

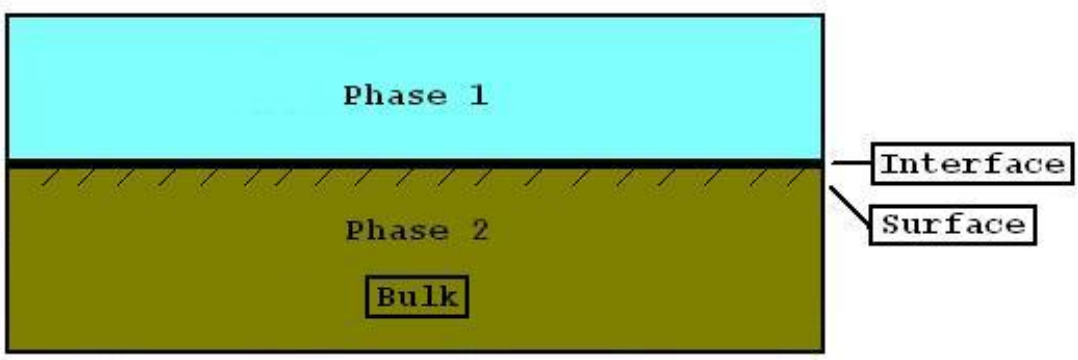

Figure 1: The interface region between two immiscible phases, Phase 1 (water) and Phase 2 (soil).

Most environmental processes in geochemical systems occur at the interface between two different phases of matter and in particular at the liquid/solid interface. It is important to study the chemistry at these interface regions to be able to answer key environmental questions. For example, the interaction of a pollutant with soil particles can be studied to determine the fate, transport and bioavailability of that pollutant. A pollutant that adsorbs poorly to soil is more mobile and can travel great distances to contaminate water supplies, while one that adsorbs strongly to soil will contaminate only small and isolated regions. Figure 2 shows a pollutant, $(CH_3)_2AsO_2$ adsorbed to a surface at the liquid/solid interface.

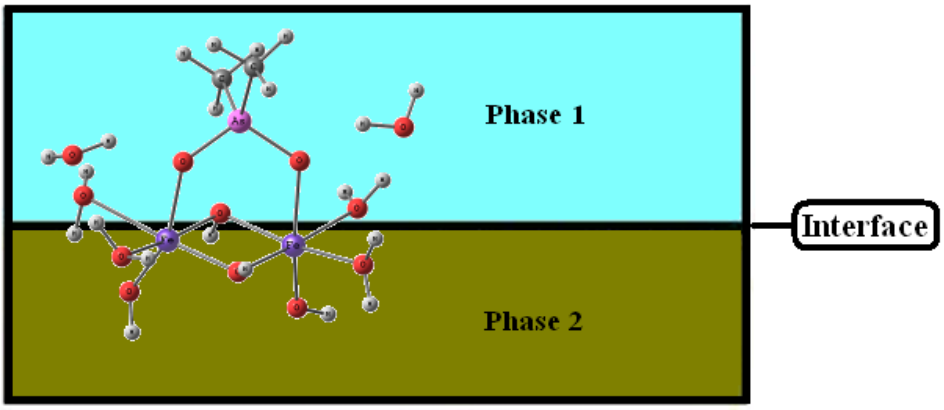

Figure 2: Adsorption of DMA on the surface of an iron oxide in the presence of water.

Similarly, remediation technologies dealing with the removal of contaminants from the environment can be designed or improved with a better understanding of the interactions at the interfacial region. For example, the use of iron oxides (goethite) in arsenic contaminated soils was found to be effective in adsorbing the pollutant and stopping the negative effects of arsenic on plant growth.[2] Similarly, to lower the content of arsenic in organic rich fuels, the washing with iron-oxide slurries and collecting of contaminated particles for recycling was suggested as an alternative to just washing with water alone.[3] Thus studies at the liquid/solid interface, especially those that include the thermodynamics of binding, become very important when trying to answer environmental questions and thinking about remediation technologies.

1.2 Arsenic in the Environment

Arsenic can be found naturally in bedrocks all around the world. It is the 20th most abundant element in the earth's crust and occurs in over 500 different mineral forms. A few common examples of arsenic containing minerals are arsenopyrite (FeAsS), realgar (AsS),

enargite (Cu_3AsS_4), orpiment (As_2S_3) and niccolite (NiAs). The natural weathering of rocks will cause arsenic to be liberated and transported by surface and groundwater. Depending on its oxidation state, arsenic species can adsorb to different types of soil containing reactive minerals.[4]

Arsenic compounds have a variety of important applications and are introduced to the environment via anthropogenic sources as well. Some examples are:

- *Chromated copper arsenate* (CCA) used in pressure treated wood to protect from rotting due to insects and microbial activity.[5]
- *Roxarsone* (ROX) and p-arsanilic acid (pAsA) are used as food additives in the poultry industry to prevent diseases and stimulate growth.[6]
- *Dimethylarsinic Acid* (DMA) and Monomethylarsonic Acid (MMA) were used historically as herbicides and pesticides.[7]
- *Gallium Arsenide* (GaAs) used as a semiconductor in various electronic devices.[8]

The last example, in particular, is becoming more important from both an engineering and environmental perspective. GaAs semiconductors provide some advantages over silicon in many applications and have been shown to be very efficient in solar devices.[9] This may increase the number of technologies that use GaAs and therefore increase the number of GaAs electronics building in landfills as the race for faster, cheaper and more efficient electronics continues.

Arsenic should also be taken very seriously for its health and environmental risks. Arsenic is extremely toxic (depending on the dose and length of exposure), a well known carcinogen[10] and the chronic exposure to arsenic in drinking water (even at small amounts)

can cause Arsenicosis.[11] This is a real and current problem in Bangladesh and various parts of China, where drinking water with arsenic concentrations higher than 100 parts per billion (ppb) have been reported.[12] For comparison, the Environmental Protection Agency (EPA) sets the arsenic standard for drinking water at 10 ppb.[13]

On top of this, arsenic compounds have also been a challenge to the energy industry. Shale oil, an alternative to crude oil, is extracted from oil shales (a sedimentary rock with high organic content) through the process of pyrolysis. Arsenic compounds are present in most oil shales at concentrations between 10 and 200 parts per million (ppm), and they can act as catalyst poisons hindering the conversion of oil shale into valuable liquid fuels.[14]

In Canada, concentrations of arsenic are significantly higher in areas with arsenic-enriched bedrock, arsenic-bearing precious metal deposits, gold production facilities, former gold-mining operations and around gold ore roasters. The Canadian Environmental Protection Act (CEPA) lists arsenic and its compounds on their Toxic Substances List and in their Assessment Report concluded that "organisms are exposed to arsenic and its inorganic compounds in Canadian surface waters, sediments, soils and biota at concentrations which may be sufficiently high to cause harmful effects".[15]

Arsenic exists in nature both in organic and inorganic forms. The most common inorganic forms of arsenic (iAs) occur at the oxidation states +3 [As(III) or Arsenite] and +5 [As(V) or Arsenate]. Inorganic As(V) is the dominant species under aerobic conditions, binding stronger to soil and being less mobile, while As(III) is the dominant species under reducing conditions, being more soluble and more mobile in the environment.

Figure 3 below shows the distribution of arsenic in the environment with varying pH and redox potential (Eh), the most important factors controlling Arsenic speciation.[16,17]

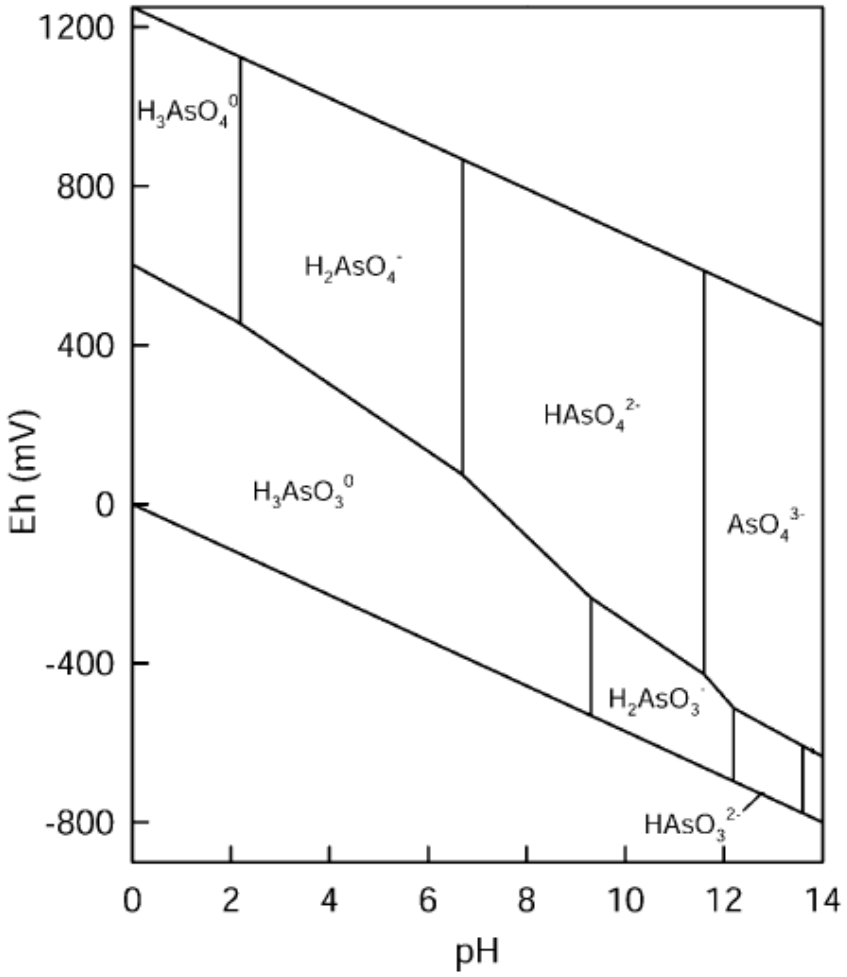

Figure 3: Eh-pH diagram for aqueous As species. As, O_2, H_2O system at 25°C and 1 bar total pressure. Reproduced from P.L. Smedley, D.G. Kinniburgh. Applied Geochemistry 17 (2002), pp. 517–568.

From Figure 3 we see that in the pH range 6 to 9, found in most natural environments, the dominant arsenate species are $H_2AsO_4^-$ and $HAsO_4^{2-}$, while the dominant arsenite species is H_3AsO_3. Microorganisms (i.e. bacteria and fungi) can biomethylate inorganic arsenic producing organic forms of arsenic, such as monomethylarsonic acid (MMA) and dimethylarsinic acid (DMA).[18]

The toxicity of arsenic varies also with the chemical form and the oxidation state of the species. Hirano et al. report the toxicity order of arsenic compounds in several cell lines as:

DMA(III), MMA(III) > iAs(III) > iAs(V) > DMA(V), MMA(V).[19]

This is illustrated in Figure 4 below.

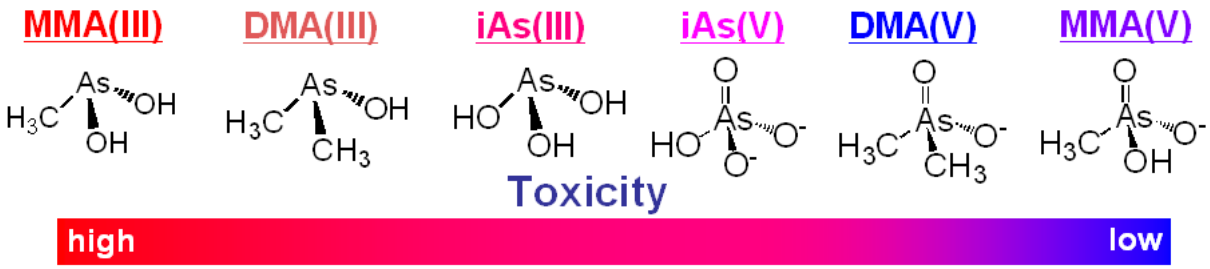

Figure 4: Toxicity order of arsenic according to chemical form and oxidation state.

DMA(V), the chemical of focus in this thesis, has been shown to have multi-organ tumour promoting activity in rodents and the trivalent form, DMA(III), is known to be highly cytotoxic and genotoxic, interacting directly with genetic material.[20] All in all, in spite of some important applications, arsenicals in both their organic and inorganic forms pose a great health and environmental risk and are a challenge to the energy industry because of their action as catalyst poisons.

For these reasons, it is necessary to understand the types of interactions taking place at the liquid/solid interface of reactive surfaces in various environmental conditions. Theoretical studies at the molecular level that use environmentally relevant materials under proper environmental conditions can increase our understanding of the kind of chemical reactions and adsorption processes that take place.

Theoretical studies can also provide some very useful information that aid in the interpretation of spectroscopic data,[21] provide geometrical parameters useful for extended X-ray absorption fine structure (EXAFS),[22] as well as increase our understanding about the mechanism of binding and the thermodynamic favorability of different surface interactions.[23] The next two sections will go into greater detail about the experimental and computational chemistry approaches we use to study surface interactions of DMA.

1.3 The Experimental Approach to Studying Surface Chemistry of Arsenicals

Attenuated Total Reflectance Fourier Transform Infrared (ATR-FTIR)[24] spectroscopy is a surface sensitive technique based on the total internal reflection of an infrared (IR) beam of light inside a crystal of high refractive index, typically Zinc Selenide (ZnSe) or Germanium (Ge). At the interface, an evanescent wave is created that extends a few microns (0.5 – 5 μm) beyond the crystal and into the sample. This is seen in Figure 5 below. Such relatively short path lengths are required for subtracting out the signal of highly IR absorbing solvents, such as water, so that signals due to solutes becomes distinguishable.

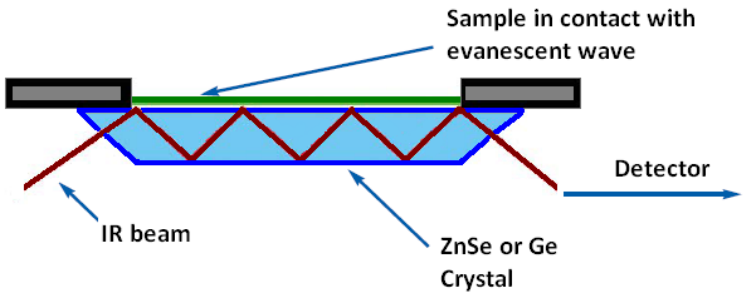

Figure 5: Totally internally reflected infrared beam in contact with a sample.

In the case of arsenate, arsenite or methylated arsenicals, like DMA, energy is absorbed due to the As-O stretching vibrations [ν(As-O)] in the 600-1000 cm^{-1} (wavenumber)

range. Since arsenic compounds bind to metal oxides through their As-O bonds, shifts in the frequency of these vibrations can be used to identify surface interactions when comparing studies performed in bulk solution and in the presence of reactive compounds such as iron oxides. Recently, results from ATR-FTIR studies of DMA adsorption on hematite (Fe_2O_3) and goethite (FeOOH) complemented by quantum chemical calculations on DMA-iron oxide clusters, have identified that there is simultaneous formation of inner- and outer-sphere complexes, each with distinct spectral components.[3]

To aid in the interpretation of ATR-FTIR data and the assignment of peaks, especially in such complex region of the IR spectrum as the fingerprint region, molecular modeling becomes very useful. To illustrate, a calculated IR spectrum for DMA [$(CH_3)_2AsO_2^-$] in water is provided in Figure 6 below. The most prominent peaks at 787 cm^{-1} and 788 cm^{-1} are assigned to the As-O anti-symmetric and As-O symmetric stretching vibrations, respectively. The other major peaks at 631 cm^{-1}, 727 cm^{-1} and 867 cm^{-1} are from water bending motions, while the minor peaks at 606 cm^{-1} and 823 cm^{-1} are from the methyl groups stretching and rocking motions respectively.

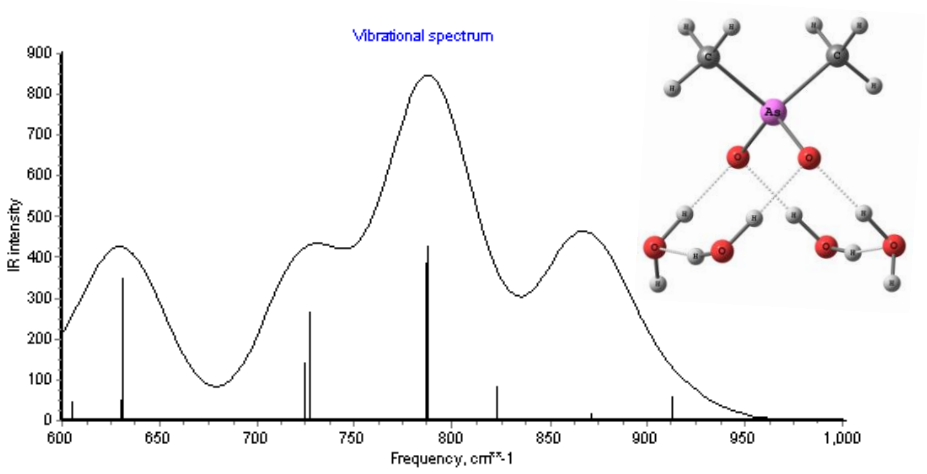

Figure 6: Calculated IR spectra for $DMA^- \cdot (H_2O)_4$ using B3LYP/6-311+G(d,p) with the IEFPCM solvation model. (IR peaks in this figure were not scaled for anharmonic behavior).

Another experimental technique is extended X-ray absorption fine structure (EXAFS) which is the part of the X-ray Absorption Spectrum (XAS) that oscillates and extends beyond the absorption edge of the element in the sample being studied. In EXAFS, electrons are knocked off when the energy of an incident X-ray exceeds the ionization energy (or the edge energy) and the outgoing photoelectrons interfere with the scattered waves from the atoms nearby. This causes constructive and destructive interference seen as maxima and minima (the oscillations) in EXAFS.[25] The way EXAFS works is shown in Figure 7 below where an electron is knocked out from the Fe atom and interferes with the scattered wave from the oxygen atom nearby.

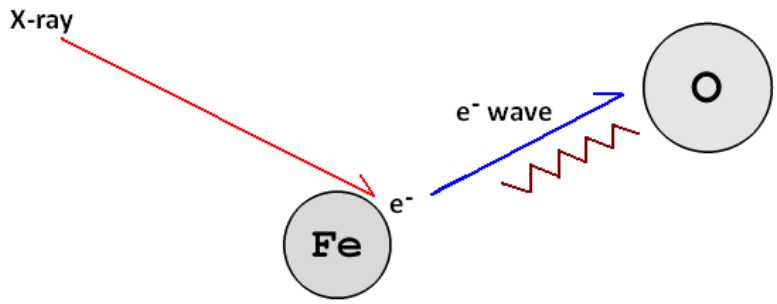

Figure 7: X-ray absorption knocking off electrons that causes oscillations seen in EXAFS

EXAFS is useful in geochemistry because it gives information about the distance between the central and neighbouring atoms, as well as the number of neighbouring atoms within a distance of 5 to 6 angstrom. For example, a study of DMA sorption onto Fe-oxides found that there are 1.9 Fe atoms located at an inter-atomic As-Fe distance of 3.30 Å.[26] The meaning of this will be discussed further in the thesis.

1.4 The Computational Approach to Studying Surface Chemistry of Arsenicals

Molecular modeling has become increasingly popular for the study of geochemical reactions and, in particular, Density Functional Theory (DFT) has become the method of choice for many geochemists.[27] DFT uses functionals of the electron density (hence the name) rather than the wave function to solve the many-electron system which reduces the many-body problem with 3N spatial coordinates (where N is the number of electrons) to only 3 spatial coordinates, thus reducing computational cost. Another benefit to DFT is that, unlike Hartree-Fock theory, it includes the effects of electron correlation (i.e. the effects and energy contributions that arise from electrons in a molecular system as they react to one another's motion and stay out of each other's way).[28]

The basic theory was formulated in 1964 by Hohenberg and Kohn which showed the existence of a functional that determines the ground state energy and density precisely, even though the theorem did not provide that functional. The work of Kohn and Sham led to methods of approximating functionals. The approximate functionals used by existing DFT methods, partition the electronic energy, E, into several components that are computed separately as shown in Equation 1.0 below,

$$E = E^K + E^V + E^J + E^{XC} \qquad \textbf{(Eqn. 1.0)}$$

where E^K is the kinetic energy arising from the movement of the electrons, E^V is the potential energy arising from nuclear-electron attraction and nuclear-nuclear repulsion, E^J is the Coulomb repulsion energy between electrons, and E^{XC} is the exchange-correlation energy accounting for the remainder of electron-electron interactions.[28] All the terms in Equation

1.0 are functions of the electron density (except of course the nuclear-nuclear repulsion term included in the potential energy).

For this thesis, various DMA-iron oxide and phosphate-iron oxide clusters were energy minimized to study adsorption/desorption interactions and to obtain details about their geometries, Gibbs energies and spectroscopic information. Numerous hypothetical ligand exchange reactions, leading to the formation of inner- and outer-sphere complexes, are also constructed and the Gibbs free energies of adsorption (ΔG_{ads}) are calculated to gain insight into the thermodynamic favorability of adsorption. Similarly, the Gibbs free energies of desorption (ΔG_{des}) are calculated for various desorption reactions of DMA in the presence of phosphate. The Gibbs free energy of adsorption/desorption is calculated using Equation 1.1 below,

$$\Delta G_{ads} = \sum(E_0 + G_{corr})_{products} - \sum(E_0 + G_{corr})_{reactants} \qquad \textbf{(Eqn. 1.1)}$$

where E_0 is the calculated total electronic energy of the system and G_{corr} is the Thermal Correction to Gibbs free energy.[29] An example for an adsorption reaction is shown in Equation 1.2 below as an adsorption to the iron oxide cluster.

$$\text{DMA-H} \cdot (H_2O)_4 + Fe_2(OH)_5(OH_2)_5^+ \cdot (H_2O)_4 \rightarrow \text{DMA-}Fe_2(OH)_4(OH_2)_4^+ \cdot (H_2O)_4 + 6(H_2O) \qquad \textbf{(Eqn. 1.2)}$$

The reaction shows how DMA-H adsorbs onto the iron oxide surface and forms a bidentate binuclear complex. To balance the stoichiometry of the reaction there are also 6 waters in the products side. It was found that treating the waters separately is more favourable than treating them as a cluster when the correction factor, G_{corr}, is added. The reaction of Eqn. 1.2 is illustrated in Figure 9 below using 3-D molecular structures,

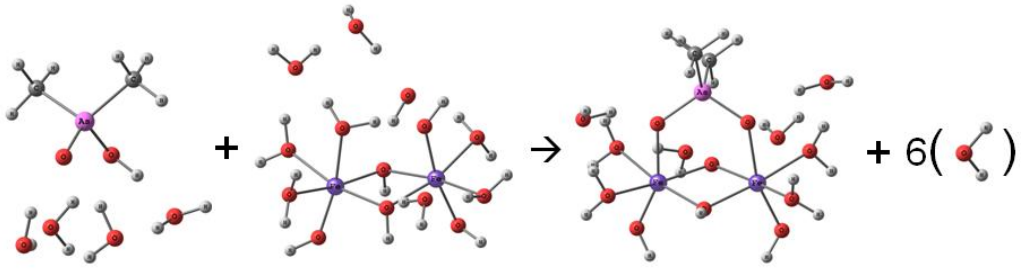

Figure 8: DMA-H reacting with an iron oxide surface to form a bidentate binuclear complex.

In a computational study of inorganic As(V) and iron oxides complexes, the bidentate binuclear (i.e. corner sharing) complex was found to be more stable by 55 kJ/mol than the bidentate mononuclear (i.e. edge sharing) complex.[30] For this reason, when considering bidentate complexation, only the reactions leading to the more stable corner sharing complex will be studied. Figure 10 below illustrates the difference between the bidentate binuclear complex of DMA on iron oxide (left) and the less stable bidentate mononuclear complex (right):

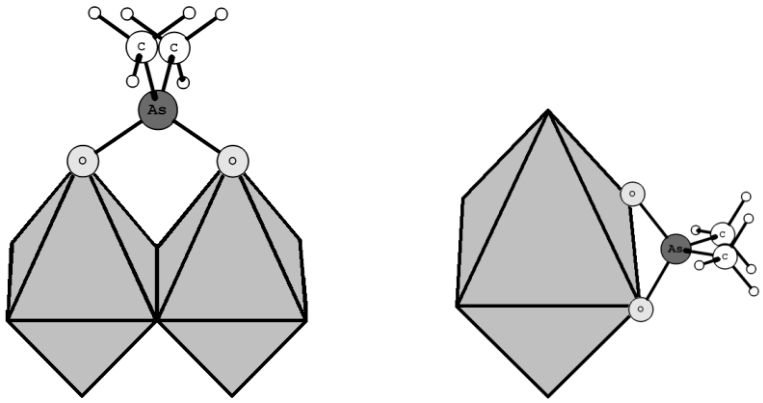

Figure 9: The corner-sharing (left) complex is more stable than the edge sharing (right) complex.

Studies by Kubicki et al[31] looking at sorption of oxyanions (including arsenate and arsenite) onto reactive Al and Fe hydroxide clusters, have identified the geometries and infrared vibrational frequencies for the complexed species and compared them to EXAFS and ATR-FTIR results, while also calculating reaction free energies for some hypothetical

complexation reactions. They concluded that DFT calculations are very useful, especially when combined with experimental work, being able to answer some fundamental questions about energies, explaining shifts (or new peaks) in vibrational frequencies when adsorption from solution onto mineral surfaces takes place and also being able to predict thermodynamic favorability for various reactions. Extending this work to include organic forms of arsenic like DMA can be very useful for the same reasons and is the main purpose of this thesis.

2 Objectives

The objectives of this thesis are to offer a detailed theoretical analysis of the interactions between DMA(V) and iron-oxide clusters. The main goals are to use density functional theory to determine the mechanism of DMA binding to reactive iron oxide clusters in an aqueous environment (mimicking the reactions that would occur at the top layer of an iron oxide surface) and identifying the types of DMA/iron oxide complexes that form.

Geometry optimization and frequency calculations are meant to complement experimental work and help with the interpretation of infrared spectroscopic data and the assignment of peaks, as well as provide geometrical parameters useful for modeling x-ray absorption data using EXAFS.

Finally, calculations of the Gibbs free energies of adsorption and desorption for various hypothetical ligand exchange reactions will allow us to make predictions about which reactions are more thermodynamically favourable and thus help us identify the types of

complexes that are more likely to form, as well as the types of complexes that are more easily desorbed.

3 Computational Methods

All calculations were performed using the program Gaussian 09, running on SHARCNET[32], typically on 8, 16, or 24 processors (depending on availability) with computation time ranging from one hour to three or four days (depending on the size of the molecule, the presence of transition metals and the number of explicit waters added). All calculations were performed at 298.15 Kelvin and 1 atmospheric pressure. Vibrational frequencies were inspected visually using ChemCraft (v.1.6) and all weak ν(As-O) were ignored since they were mostly caused by other motions in the molecule. The medium and strong ν(As-O) were considered meaningful and tabulated.

The methods used for the calculations in this study are B3LYP/6-31G(d), B3LYP/6-311+G(d,p) and BMK/6-311+G(d,p) where B3LYP[33], BMK[34] are the functionals and 6-31G(d), 6-311+G(d,p) are the basis sets. B3LYP and BMK are known as hybrid functionals because their exchange functional includes a mixture of Hartree-Fock exchange and DFT exchange-correlation. The basis set is a mathematical representation of the molecular orbitals or electron density of a system and therefore it restricts the electrons to a particular region of space. The smaller basis sets have more constraints on the electrons while the larger basis sets have fewer constraints on the electrons and can give a more accurate approximation of the real molecular orbitals or electron density. The 6-31G(d) uses polarization functions for heavy atoms, which allows the orbitals to change size and shape, with the “d” indicating that

d functions are added to heavy atoms. The larger basis set 6-311+G(d,p) also adds diffuse functions to the system as indicated by the "+", p functions to hydrogen atoms as indicated by the "p" and extra valence functions as indicated by the extra "1".[35] To sum up, the larger basis set should give better results and, unless otherwise specified, the 6-311+G(d,p) basis set will be the one used in this thesis for discussion and comparison with experimental results.

In order to properly mimic DMA molecules in a hydrated environment, waters are added explicitly around the structure and calculations are performed using a solvation model. The two solvation models used in this study are the integral equation formalism polarizable continuum model (IEFPCM) [36] and the universal solvation model (SMD)[37], which is an extension of the IEFPCM. For both of these solvation models, a cavity is formed as a set of spheres around each atom to represent the volume occupied by the solute, followed by the cavity being placed in a medium that imitates a solvent.[32,38] This is illustrated in Figure 8, showing DMA with four explicit waters placed in a continuous dielectric medium to mimic solvation effects. The solvent used in this study is water (i.e. the solvent has a dielectric constant, ε, equal to that of water).

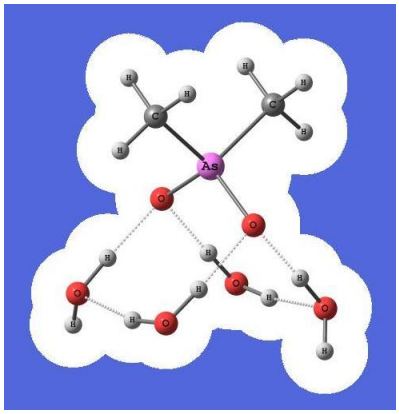

Figure 10: A solvated DMA molecule surrounded by explicit waters in a solvation model

The region where the solvent molecules interact with the solute (also known as the cybotactic region) has properties that are different from the bulk and therefore the use of explicit waters in the calculations is required to deal with first solvation shell effects such as hydrogen bonding, whereas the implicit use of a solvation model accounts for other effects such as ion-dipole and dipole-dipole interactions. The choice for having 4 explicit waters surrounding each structure and complex is explained in Appendix A.

For clusters that contain two Fe^{3+} atoms, calculations were performed at high spin with a Multiplicity 11 (i.e. 10 unpaired electrons) because this produced the lowest energy. It was found that the lowest energy, for iron oxide systems containing Fe^{3+}, occurred when the Multiplicity was set to 5N+1, where N is the number of Fe^{3+} atoms in the system (i.e. 5 unpaired electrons for each Fe^{3+} atom). Clusters with one and three Fe^{3+} atoms were also considered, with the lowest energy at multiplicity 6 and 16 respectively (following the observed 5N+1 rule). For this study, only the clusters with two Fe^{3+} atoms were considered since they allow the formation of corner sharing (bidentate binuclear) complexes and are less computationally expensive than clusters having more than two iron atoms.

It was also observed that having more than three OH ligands on the Fe^{3+} atom produces a change in the coordination geometry of the iron hydroxide, forming a 4-fold (tetrahedral) geometry in less hydrated environments or a 5-fold (trigonal bipyramidal) geometry as more water molecules are added around the iron hydroxide. This is consistent with other computational work on Fe^{3+} atoms.[39] For all other complexes, where the Fe^{3+} atom had three or fewer OH ligands, the octahedral coordination geometry was found to be stable.

4 Results and Discussions

4.1 Optimized Geometries of Aqueous and Complexed DMA

The optimized geometries of the various DMA species used in this study are shown in Figure 11 as structures a, b and c.

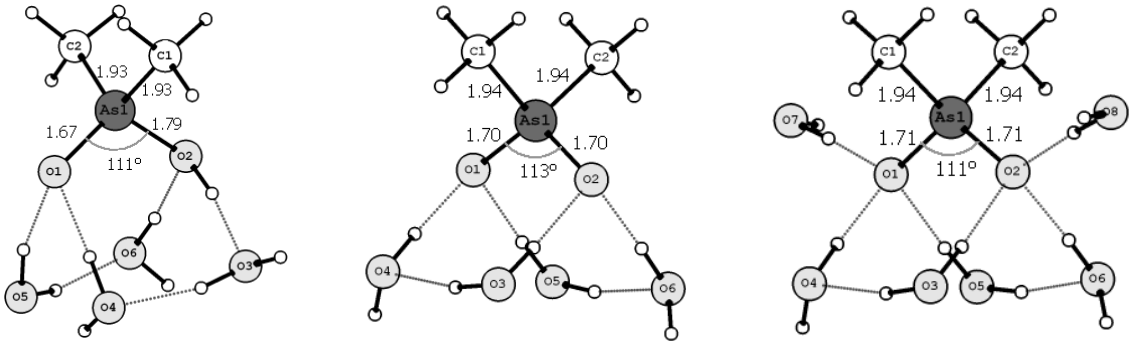

a. DMA-H · $(H_2O)_4$ **b.** DMA^- · $(H_2O)_4$ **c.** DMA^- · $(H_2O)_6$

Figure 11: Optimized structures of DMA-H and DMA^- surrounded by four (a, b) or six (c) explicit waters. Calculated using B3LYP/6-311+G(d,p) and the IEFPCM solvation model.

The calculated As-O bond distances, d(As-O), for the structures shown in Figure 11 ranged between 1.69 – 1.72 angstrom (Å) for the deprotonated form of DMA and between 1.67 and 1.69 Å for the protonated form DMA-H, whereas the As-OH bond ranged between 1.77 and 1.79 Å depending on the method of calculation. The d(As-O) values are shown in Table 1 for all the four methods considered in this study, with the B3LYP/6-311+G(d,p) with IEFPCM as the preferred method in bold.

Table 1: As-O bond distances (Å) of DMA in water (structures a, b and c from Figure 11)

	DMA^- · $(H_2O)_4$		**DMA^- · $(H_2O)_6$**		**DMA-H · $(H_2O)_4$**	
Method	As-O_1	As-O_2	As-O_1	As-O_2	As-O_1	As-OH
B3LYP/6-31G(d) with IEFPCM	1.69	1.69	1.70	1.70	1.67	1.77
B3LYP/6-311+G(d,p) with IEFPCM	**1.70**	**1.70**	**1.71**	**1.71**	**1.67**	**1.79**
B3LYP/6-311+G(d,p) with SMD	1.71	1.71	1.72	1.72	1.69	1.79
BMK/6-311+G(d,p) with IEFPCM	1.69	1.69	1.69	1.69	1.66	1.77

Having four explicit water molecules allows only 4 hydrogen bonds to form between DMA and the surrounding waters, while having six waters allows for 6 hydrogen bonds to form. The effects of that can be seen in Figure 12 below. There is a slight change in d(As-O) from 1.70 Å to 1.71 Å when the two extra waters are present, as well as an increase in the hydrogen bond distances raging from 1.68 – 1.82 Å in the case with four waters and from 1.72 – 1.85 Å in the case with six waters. The As-C bond distances, d(As-C), remain the same at 1.94 Å for both cases, while the O-As-O angle changes slightly from 113° to 111°. See Appendix A for a more detailed study about the effects of adding explicit waters.

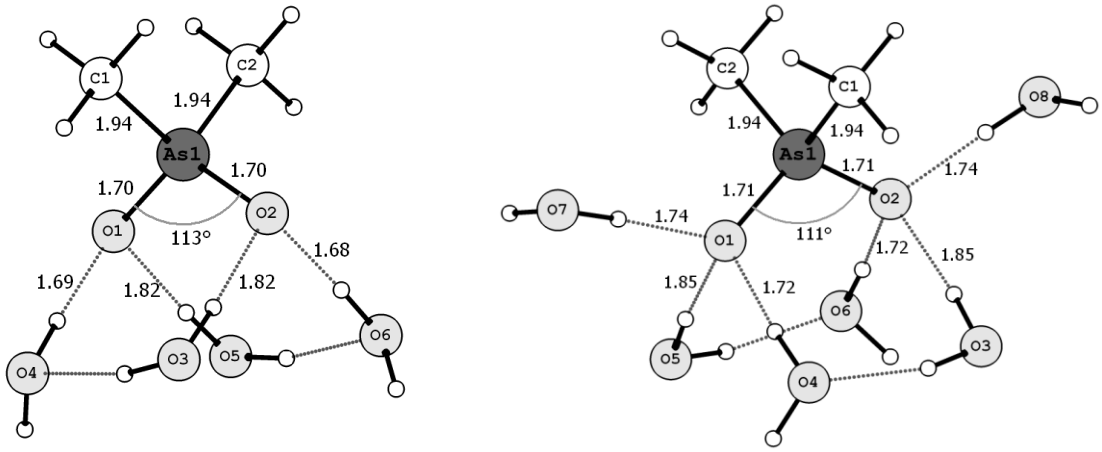

$DMA^- \cdot (H_2O)_4$ $DMA^- \cdot (H_2O)_6$

Figure 12: The geometries and hydrogen bonds when DMA^- is surrounded by four (left) and six (right) explicit waters. Calculated with B3LYP/6-311+G(d,p) and the IEFPCM solvation model.

The optimized geometries of the iron hydroxide clusters with which DMA will react are shown in Figure 13 as structures d and e. The optimized geometries in Figures 11 and 13 (structures a through e) are those of the reactants which lead to the formation of DMA-iron oxide complexes A through F in Figures 14, 15 and 16.

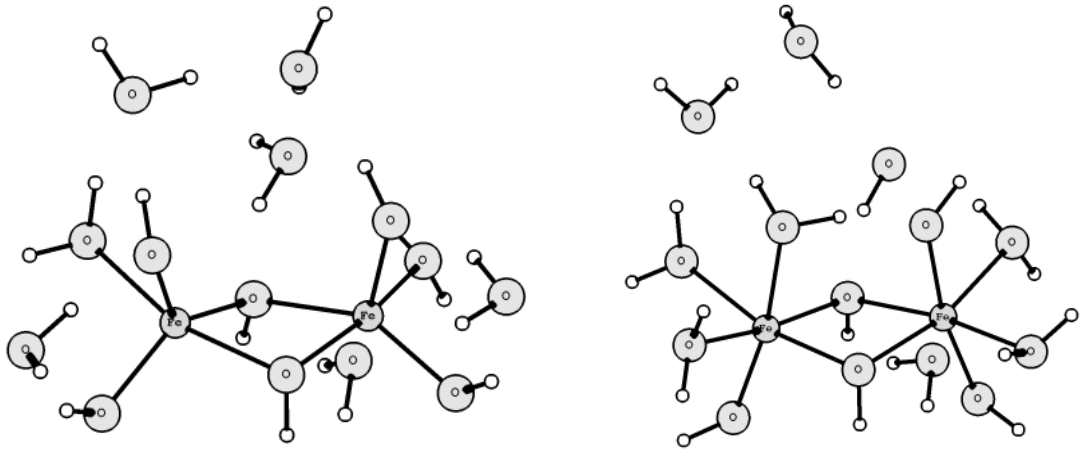

d. $Fe_2(OH)_6(OH_2)_2 \cdot (H_2O)_6$ **e.** $Fe_2(OH)_5(OH_2)_5^+ \cdot (H_2O)_4$

Figure 13: Optimized iron hydroxide neutral (d) cluster and positively charged (e) cluster with surrounding water molecules. Calculated with B3LYP/6-311+G(d,p) and the IEFPCM solvation model.

The optimized geometries of the neutral (A) and positively charged (B) monodentate (MD) complexes are shown in Figure 14 below.

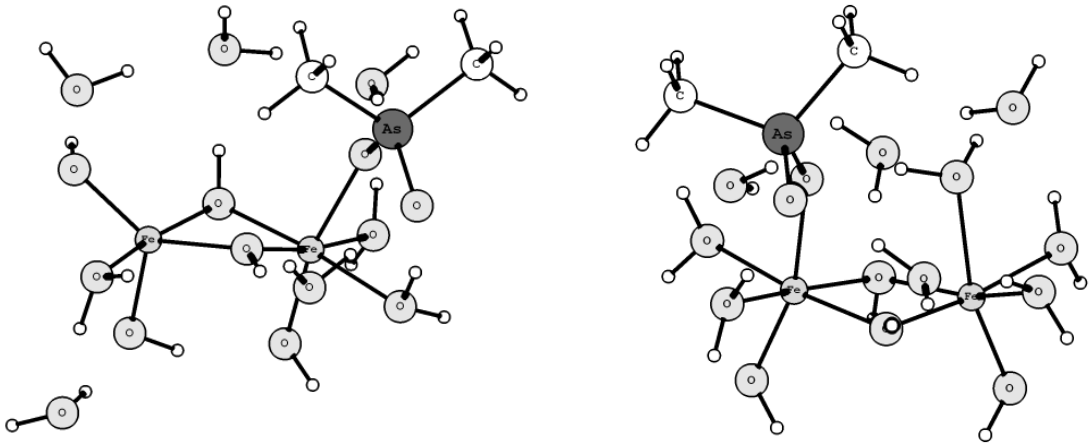

A. DMA-$Fe_2(OH)_5(OH_2)_3 \cdot (H_2O)_5$ **B.**DMA-$Fe_2(OH)_4(OH_2)_5^+ \cdot (H_2O)_4$

Figure 14: Optimized MD neutral (A) and positively charged (B) complexes surrounded by water molecules. Calculated with B3LYP/6-311+G(d,p) and the IEFPCM solvation model.

The optimized geometries of the neutral (C) and positively charged (D) bidentate (BD) complexes are shown in Figure 15 below.

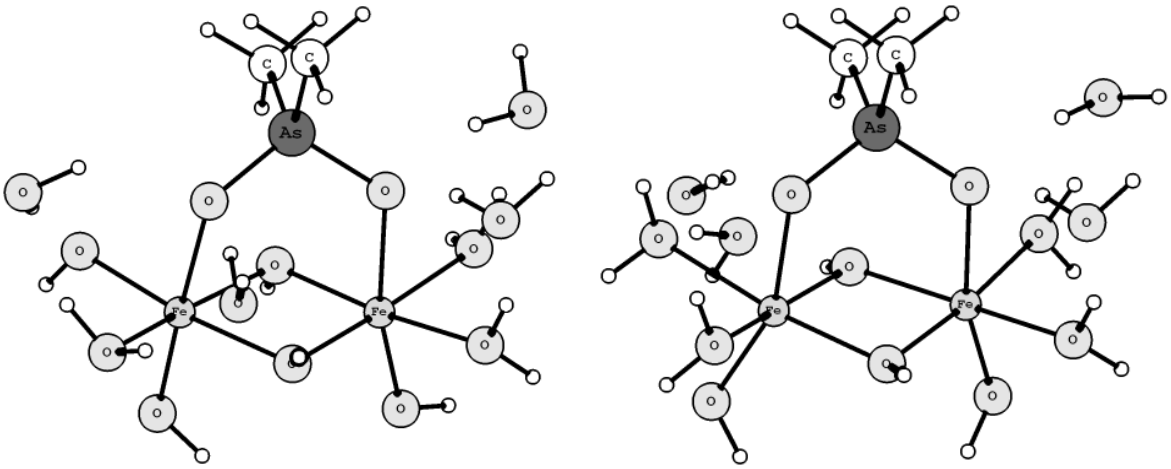

C. DMA-$Fe_2(OH)_5(OH_2)_3 \cdot (H_2O)_4$ **D.** DMA-$Fe_2(OH)_4(OH_2)_4^+ \cdot (H_2O)_4$

Figure 15: Optimized BD neutral (C) and positively charged (D) complexes surrounded by water molecules. Calculated with B3LYP/6-311+G(d,p) and the IEFPCM solvation model.

Likewise, the optimized geometries of the neutral (E) and positively charged (F) outer-sphere (OS) complexes are shown in Figure 16 below.

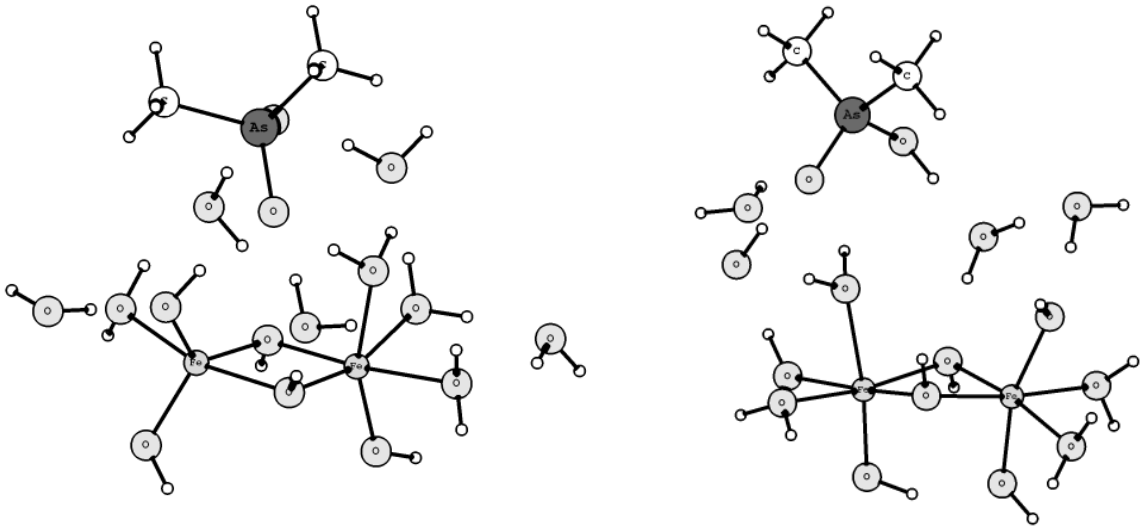

E. DMA $\cdot (H_2O)_5$ $Fe_2(OH)_5(OH_2)_4$ **F.** [DMA-H $\cdot (H_2O)_4$ $Fe_2(OH)_5(OH_2)_5]^+$

Figure 16: Optimized OS neutral (E) and positively charged (F) complexes surrounded by water molecules. Calculated with B3LYP/6-311+G(d,p) and the IEFPCM solvation model.

The atomic d(As-O) and inter-atomic d(As-Fe) distances of complexes A through F in Figures 14, 15 and 16 are posted in Table 2 below. The B3LYP/6-311+G(d,p) IEFPCM method

(in bold) will be the only method considered in the analysis and all other methods will be discussed in comparison to it.

Table 2: As-O bond distances and As-Fe inter-atomic distances (Å) of DMA/iron oxide complexes A – F

Monodentate Complexes	**Complex A - MD, Charge 0**				**Complex B - MD, Charge 1**			
	As-O_1	As-OFe	As-Fe_1	As-Fe_2	As-O_1	As-OFe	As-Fe_1	As-Fe_2
B3LYP/6-31G(d) IEFPCM	1.70	1.72	3.28	4.86	1.71	1.73	3.42	4.90
B3LYP/6-311+G(d,p) IEFPCM	**1.68**	**1.73**	**3.43**	**4.89**	**1.71**	**1.74**	**3.45**	**4.94**
B3LYP/6-311+G(d,p) SMD	1.71	1.75	3.25	5.50	1.70	1.75	3.32	5.17
BMK/6-311+G(d,p) IEFPCM	1.68	1.72	3.33	4.92	1.68	1.73	3.43	4.89
Bidentate Complexes	**Complex C - BD, Charge 0**				**Complex D - BD, Charge 1**			
	As-O_1	As-O_2	As-Fe_1	As-Fe_2	As-O_1	As-O_2	As-Fe_1	As-Fe_2
B3LYP/6-31G(d) IEFPCM	1.72	1.70	3.32	3.40	1.71	1.73	3.41	3.14
B3LYP/6-311+G(d,p) IEFPCM	**1.74**	**1.71**	**3.36**	**3.43**	**1.73**	**1.72**	**3.39**	**3.30**
B3LYP/6-311+G(d,p) SMD	1.73	1.73	3.27	3.32	1.72	1.74	3.53	3.16
BMK/6-311+G(d,p) IEFPCM	1.72	1.70	3.31	3.38	1.71	1.70	3.33	3.28
Outer Sphere Complexes	**Complex E - OS, Charge 0**				**Complex F - OS, Charge 1**			
	As-O_1	As-O_2	As-Fe_1	As-Fe_2	As-O_1	As-OH	As-Fe_1	As-Fe_2
B3LYP/6-31G(d) IEFPCM	1.70	1.71	5.19	4.64	1.69	1.74	5.57	6.44
B3LYP/6-311+G(d,p) IEFPCM	**1.70**	**1.71**	**5.28**	**4.84**	**1.69**	**1.76**	**5.75**	**6.84**
B3LYP/6-311+G(d,p) SMD	1.71	1.72	5.02	5.05	1.70	1.77	5.84	6.23
BMK/6-311+G(d,p) IEFPCM	1.69	1.70	5.29	4.75	1.67	1.75	5.79	6.63

Distances for the As-O bonds ranged between 1.68 to 1.74 Å in complexes A through E, while the d(As-OH) was calculated to be 1.76 Å in Complex F. Interatomic As-Fe distances for the calculated MD complexes A and B ranged between 3.43 and 4.94 Å, while for the bidentate complexes C and D they ranged between 3.30 to 3.43 Å. Experimentally, EXAFS studies for DMA on goethite also concluded that 1.9 Fe atoms were located at an As-Fe inter-atomic distance of 3.30 Å which is indicative of DMA-goethite bidentate complexation.[40] Figure 17 shows the optimized geometry of Complex D with a similar 3.30 Å inter-atomic d(As-Fe) as the EXAFS study (explicit waters removed).

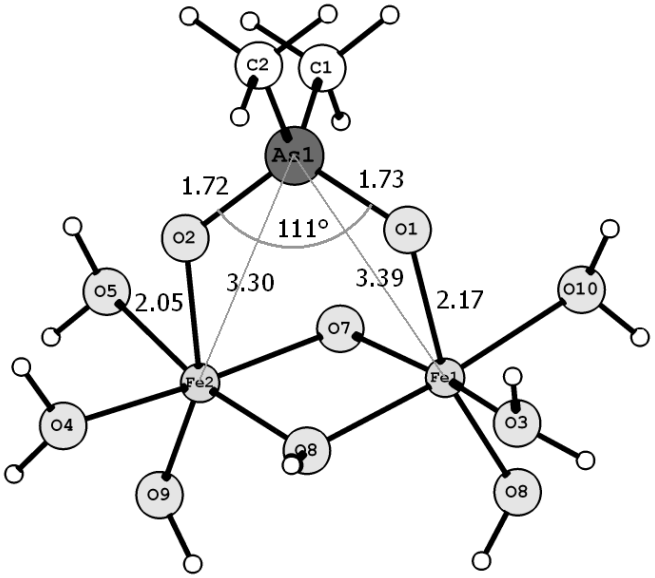

Figure 17: The geometry of DMA-$Fe_2(OH)_4(OH_2)_4^+$ (Complex D). Explicit waters removed for simplicity.

Outer-sphere complexes could not be detected by EXAFS spectroscopy due to the longer (> 5 Å) inter-atomic As-Fe distances, but have been identified by FTIR studies and DFT calculations.[3] Calculations of outer sphere Complexation (Complexes E and F) give As-Fe distances ranging from 4.84 to 6.84 Å.

From Table 2 it also is observed that changing the functional (B3LYP vs. BMK) has less effect on the geometries of the complexes than changing the solvation model (IEFPCM vs. SMD). Changing from the IEFPCM to the SMD solvation model also changes the coordination geometry of the complexes in some instances. The complexes A through F optimized using B3LYP/6-311+G(d,p) with the SMD solvation model are shown in Appendix B.

4.2 Optimized Geometries of Aqueous and Complexed iAs(V)

Calculations of inorganic arsenic acid (H_3AsO_4) also have been performed at the B3LYP/6-311+G(d,p) level of theory to compare to the organic DMA structures and see the difference the two methyl groups have on the system. Since arsenic acid has a pKa_2 of 6.94[41] the dominant species in the environment will be $HAsO_4^{-2}$ in neutral/slightly basic environments and $H_2AsO_4^-$ in acidic environments. The optimized geometries of these two species are shown in Figure 18 below.

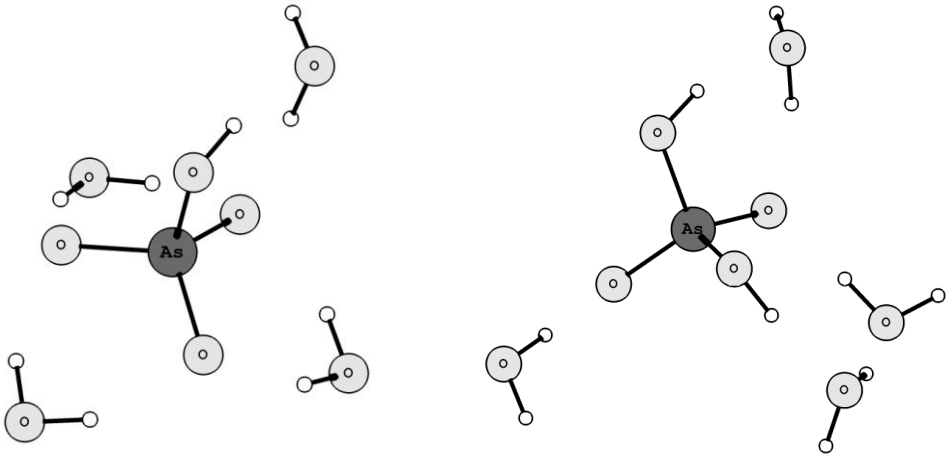

f. $HAsO_4^{-2} \cdot (H_2O)_4$ **g.** $H_2AsO_4^- \cdot (H_2O)_4$

Figure 18: The optimized geometries of arsenic acid species $HAsO_4^{-2}$ and $H_2AsO_4^-$ surrounded by four explicit waters. Calculated using B3LYP/6-311+G(d,p) and the IEFPCM solvation model.

The As-O bond distances for the two inorganic arsenic species, $HAsO_4^{-2}$ and $H_2AsO_4^-$ in water, are shown in Table 3 below.

Table 3: The As-O bond distances (Å) of arsenic acid species

Species	As=O	As-O_1	As-O_2	As-OH
f. $HAsO_4^{-2} \cdot (H_2O)_4$	1.69	1.69	1.71	1.82
g. $H_2AsO_4^- \cdot (H_2O)_4$	1.66	1.68	1.78	1.78

The optimized geometries of the neutral and positively charged complexes with inorganic arsenic on iron oxide are shown in Figure 19 below as complexes G and H.

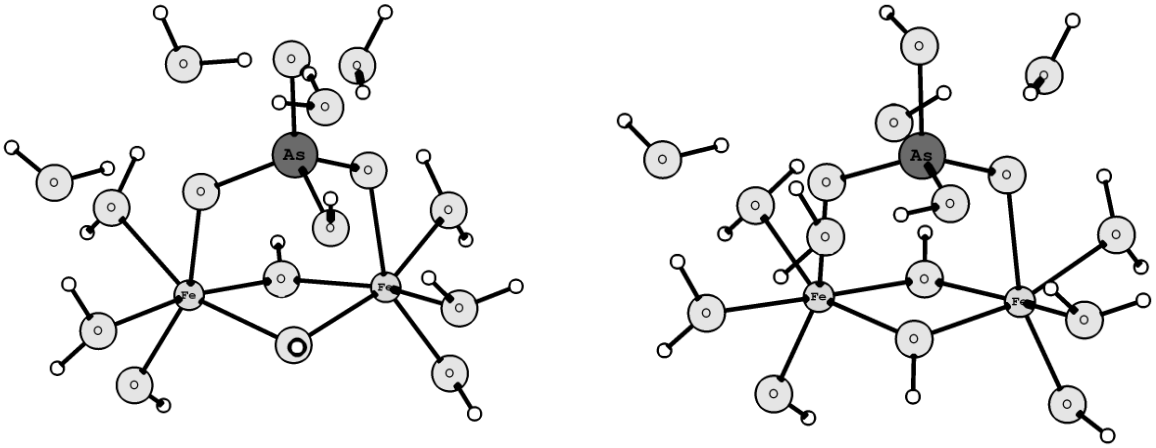

G. $HAsO_4$-$Fe_2(OH)_4(OH_2)_4 \cdot (H_2O)_4$ **H.** H_2AsO_4-$Fe_2(OH)_4(OH_2)_4^+ \cdot (H_2O)_4$

Figure 19: Optimized inorganic arsenic and iron oxide complexes, the neutral (G) and positively charged (H) complex. Calculated with B3LYP/6-311+G(d,p) and the IEFPCM solvation model.

The As-O bond distance and the inter-atomic As-Fe distances for complexes G and H are listed in Table 4 below.

Table 4: The As-O bond distances and As-Fe inter-atomic distances (Å) of complexes G and H

Inorganic Complexes	As-O_1	As-O_2	As-OFe_1	As-OFe_2	As-Fe_1	As-Fe_2
G. $HAsO_4$-$Fe_2(OH)_4(OH_2)_4 \cdot (H_2O)_4$	1.66	1.81	1.72	1.71	3.28	3.34
H. H_2AsO_4-$Fe_2(OH)_4(OH_2)_4^+ \cdot (H_2O)_4$	1.74	1.76	1.68	1.68	3.26	3.33

Calculations for the inorganic complexes show a smaller As-O(Fe) bond distance of 1.68 – 1.72 Å when compared to the organic DMA system 1.71 – 1.73 Å, as well as shorter inter-atomic As-Fe distances of 3.26 – 3.34 Å, compared to the 3.30 – 3.43 Å in the DMA complexes. The geometries of the positively charged complexes D (organic) and H (inorganic) are shown in Figure 20 for comparison.

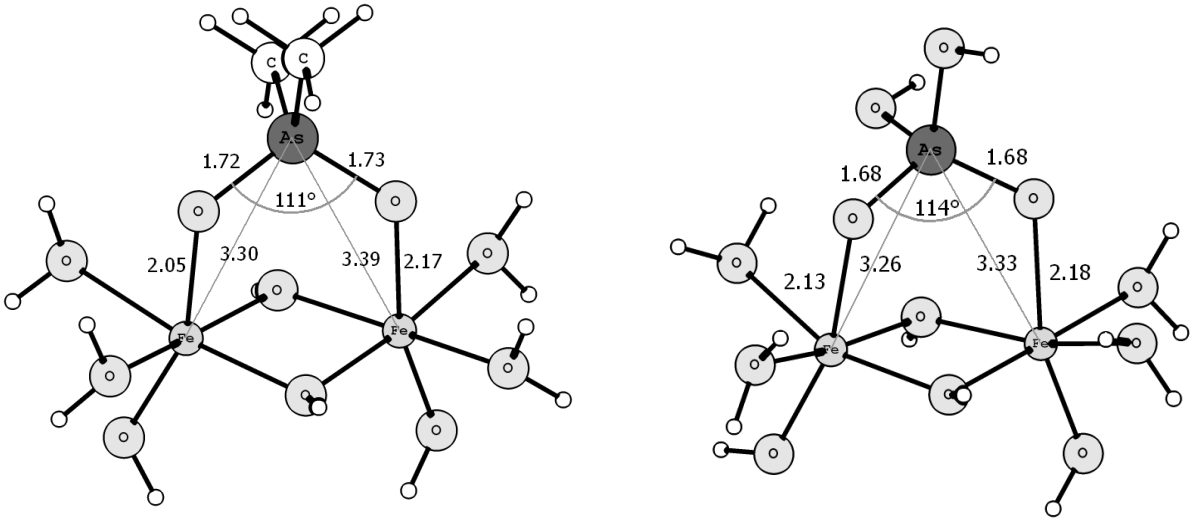

D. DMA-$Fe_2(OH)_4(OH_2)_4^+ \cdot (H_2O)_4$ **H.** H_2AsO_4-$Fe_2(OH)_4(OH_2)_4^+ \cdot (H_2O)_4$

Figure 20: Comparison between the organic DMA(V) and inorganic As(V) complexes with iron oxide. Calculated with B3LYP/6-311+G(d,p) and IEFPCM solvation model. Waters removed for simplicity.

4.3 Spectroscopic Analysis of Aqueous and Complexed DMA

Molecules vibrate at specific frequencies in response to absorbing infrared light. The spectral range considered in this study is the 600 to 1000 cm^{-1} range in the fingerprint region. This range contains the As-O stretching vibration or ν(As-O). The ν(As-O) is perfect for studying Surface Complexation because it is sensitive to binding to metal-oxides, as well as to protonation and hydrogen bonding. For example, FTIR studies of DMA adsorption onto amorphous aluminum oxide (AAO) show the major peak ν(As-O) at 880 cm^{-1} of DMA in the bulk shifting to 830 cm^{-1} when DMA is adsorbed to AAO and the peak of ν(As-OH) at 729 cm^{-1} in the bulk disappears entirely when DMA is adsorbed to AAO.[42] The ν(As-OH) peak disappears because there are no As-OH bonds in bidentate DMA/AAO complexes, while the red shift in wavenumber (Δw) of -50 cm^{-1} from 880 to 830 cm^{-1} is caused by ν(As-O) becoming ν(As-OAl) in the adsorbed DMA/AAO complex.

Vibrational frequencies are proportional to the square root of the force constant, k, divided by the reduced mass, μ, as shown in Equation 4.1 below.

$$\text{Frequency} \propto \sqrt{\frac{k}{\mu}} \qquad \textbf{(Eqn. 4.1)}$$

The calculated vibrational frequencies in this study have been corrected for anharmonicity by the multiplication of a scaling factor, F. A scaling factor that reduces the calculated frequencies by 4% is used for all four methods similar to other complexation studies performed by Kubicki et al.[44]

The importance of adding explicit waters around the complexes and their effects on the As-O stretching frequencies (without any scaling factors) are shown in Table 5, where 0 to 6 waters are added around Complex D. From Table 5 we observe that adding 4 explicit waters is adequate for this study. There is very little variability in the frequencies when going beyond 4 waters (note the 747 and 786 cm^{-1} peaks) with the extra water molecules ending up in the second solvation shell and having only minor effects on the complexes. Adding more than 4 explicit water molecules would thus make for unneeded expensive computations. For a more detailed study about the effects of explicit waters see Appendix A.

Table 5: Effects of explicit waters on ν(As-O) frequencies.

Complex	Frequencies (cm^{-1})
Complex D – 0 Waters	785, 804
Complex D – 1 Water	772, 804
Complex D – 2 Waters	772, 791
Complex D – 3 Waters	739, 780, 795
Complex D – 4 Waters	**747, 786**
Complex D – 5 Waters	**747, 785**
Complex D – 6 Waters	704, **750, 790**

The vibrational frequencies of all medium and strong ν(As-O) were calculated for structures a and b and complexes A through F using the methods B3LYP/6-311+G(d,p) with the IEFPCM and SMD solvation models as well as BMK/6-311+G(d,p) with IEFPCM and they are shown in Table 6 below. The uncorrected ν(As-O) frequencies for all four methods are presented in Appendix D.

Since DMA has a pK_a = 6.2, both the protonated and deprotonated species will be present at environmental pH levels, with DMA-H dominating the acidic environments and DMA^- dominating the neutral and slightly basic environments. For the hydrated DMA^- species, the ν(As-O) are predicted around 807-834 cm^{-1} with B3LYP/6-31G(d) and 756 cm^{-1} with B3LYP/6-311+G(d,p), while for the protonated DMA-H species, the predicted frequencies are at 885 cm^{-1} for ν(As-O) and 698 cm^{-1} for ν(As-OH) when using B3LYP/6-31G(d) and at 815 cm^{-1} for ν(As-O) and 641 cm^{-1} for ν(As-OH) when using B3LYP/6-311+G(d,p). Clearly, using the same scaling factors for both methods is not adequate, but the data can still be used to calculate redshifts in the signal when DMA adsorbs to the iron oxide. For all B3LYP methods, there is a redshift in the signal, Δw, between -30 and -50 cm^{-1} for inner-sphere complexes A through D when compared to ν(As-O) of DMA in the bulk. The BMK data shows very similar results for ν(As-O), with a slightly higher redshift Δw between -30 to -60 cm^{-1}.

The redshift for outer sphere complexes is not as prominent, since there is no direct bond to iron but it is still significant with a Δw between -10 and -20 cm^{-1} for complexes E and F as predicted by the B3LYP methods. When using the BMK method, slightly higher redshifts with Δw values between -20 and -30 cm^{-1} are observed when complexation takes place.

Table 6: Calculated ν(As-O) frequencies (cm^{-1}) of Structures a, b and Complexes A to F. Calculated with a scaling factor of 0.9600 (i.e. a reduction of calculated frequencies by 4%)

Complex	B3LYP 6-31G(d) IEFPCM	B3LYP 6-311+G(d,p) IEFPCM	B3LYP 6-311+G(d,p) SMD	BMK 6-311+G(d,p) IEFPCM
DMA-H · $(H_2O)_4$	698 871 885	641 815	624 777	677 842
DMA^- · $(H_2O)_4$	807 829 834	756 756	717 727 768	790
MD Complex A Charge 0	795 800	724 768	692 748	768 794
MD Complex B Charge +1	769 797 807	710 740 759 782	706 769 783	748 763 795 816
BD Complex C Charge 0	775 819	709 760	711 746	766 798
BD Complex D Charge +1	771 781 804	717 755	708 730	725 781 800
OS Complex E Charge 0	789 805 817	733 742 756 758	716 732 740 752	774 786 820
OS Complex F Charge +1	749 849 852	685 782 804 810	657 756 797	720 828

ATR-FTIR adsorption studies of DMA on hematite (Fe_2O_3) and goethite (FeOOH) shows ν(As-O) frequencies at 775, 793, 816, 840 and 877 cm^{-1} for the DMA/hematite complex and 768, 787, 837 and 876 cm^{-1} for the DMA/goethite complex.[3] Clearly the data that best correlates with experimental results is the B3LYP/6-31G(d) since the scaling factors used to correct for anharmonicity were designed for this method. This issue is addressed at the end of the thesis and a way for calculating scaling factors for the methods using the 6-311+G(d,p)

is described. Figure 21 shows the experimental data for DMA/hematite at a pH of 4 (grey) and 7 (black).

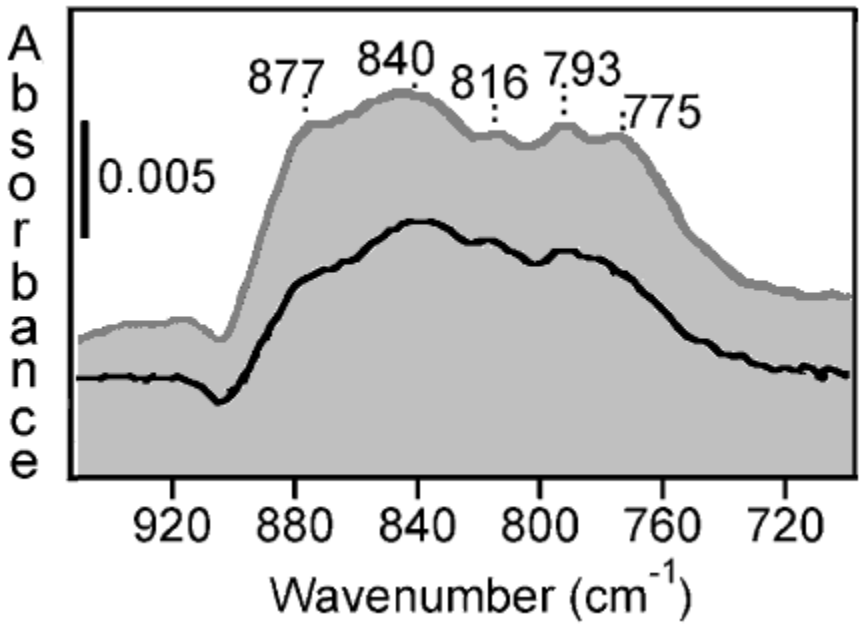

Figure 21: The ATR-FTIR adsorption spectra of DMA/hematite with experimental values at pH=4 (grey) and pH=7 (black). Data reproduced from *Environ. Sci. Technol.*, 2010, *44* (20), pp 7802–7807 (see figures in Reference 3).

From the data shown in Figure 21 it was hypothesized from the various peaks and the width of those peaks that there is simultaneous formation of both inner-sphere (bidentate and monodentate) as well as outer-sphere complexation of DMA on hematite and goethite taking place.[3] This is confirmed with DFT calculations using B3LYP/6-31G(d) showing the corrected peaks matching experimental peaks. Since the scaling factors were designed for the B3LYP/6-31G(d) method with IEFPCM, for the rest of this section only this method will be considered.

Starting with the calculated frequencies for the monodentate complexes in Table 6 there are strong As-O stretching vibrations at 795 and 800 cm^{-1} in Complex A and 769 cm^{-1}

and 797 cm^{-1} for Complex B arising from ν(As-OFe) and ν(As-O) respectively. These stretching vibrations are comparable to the 775, 793 and 768, 787 cm^{-1} observed experimentally from DMA/hematite and DMA/goethite respectively[3] and they are therefore assigned to monodentate complexes.

The calculated ν(As-OFe) for the bidentate complexes show strong As-O stretching vibrations at 775, 819 cm^{-1} for neutral Complex C and 771, 781, 804 cm^{-1} for charged Complex D, with the strongest peak being the 781 cm^{-1}. This is comparable to the, 775 and 816 cm^{-1} experimental peaks of DMA/hematite and therefore these peaks are assigned to bidentate complexes. Note that for bidentate complexes there are no ν(As-O) frequencies (i.e. all DMA oxygen atoms are bonded to iron) and all the peaks are redshifted to the 771 - 819 cm^{-1} region of the spectrum as seen in all the calculations in Table 6. Therefore it is reasonable to conclude that all peaks beyond 820 cm^{-1} come from monodentate and/or outer-sphere complexes. This can also be observed experimentally in the desorption experiment of DMA/hematite shown in Figure 22, where phosphate is used as the desorbing agent.

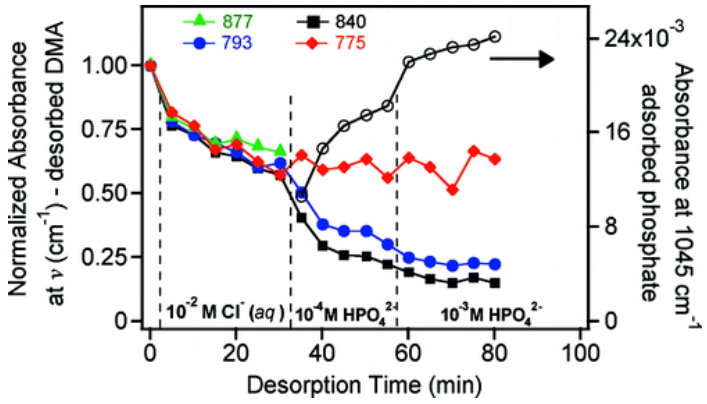

Figure 22: Desorption of DMA from hematite when flowing phosphate as a function of time. Reprinted with permission from *Environ. Sci. Technol.*, 2010, *44* (20), pp 7802–7807. Copyright 2010 American Chemical Society.

Figure 22 shows the DMA peaks decreasing (due to desorption) as a function of time, as the phosphate peak at 1045 cm^{-1} is increasing (due to phosphate complexation) as a function of time. Note that the peaks at 840 and 793 cm^{-1} are decreasing while the peak at 775 cm^{-1} levels off after some 35 minutes of flowing phosphate. This indicates the peak at 775 cm^{-1} arises from more strongly bonded inner-sphere complexes, whereas the other peaks have major contributions from outer-sphere complexes. The DFT calculations of frequencies in Table 6 confirm that the 775 cm^{-1} peak comes from the bidentate complexes (hence the strong adsorption) and that the 793, 840 cm^{-1} peaks belong to both monodentate and outer-sphere complexes respectively. Also note that the peak at 877 cm^{-1} is not being analyzed after 30 minutes because of the contribution that adsorbed phosphate has to that peak, but when another desorbing agent such as chloride is used, the 877 cm^{-1} peak is reduced in the same manner as the others peaks at 793 and 840 cm^{-1}, indicating the same type of weaker adsorption.[3] Although the peak at 816 cm^{-1} was not analyzed in the desorption study, our DFT calculations would predict a similar resistance to desorption as the 775 cm^{-1} peak because of its main contribution coming from the bidentate complexes (e.g. See Complex C in Table 6 showing ν(As-OFe) stretching at 819 cm^{-1}). The way theoretical data correlates with experiment is represented in Figure 23 below with the diagonal representing the one-to-one line.

Outer-sphere DMA complexes have no direct covalent bonds and are only hydrogen bonded to the iron oxide surface as seen in Figure 16. Complex F shows theoretical ν(As-O) frequencies at a higher wavenumber (849 and 852 cm^{-1}) due to maintaining more of the double bond As=O character, whereas inner-sphere complexes lose the double bond

character due to the formation of a resonance hybrid (i.e. delocalization of electrons). These are closer in value to the experimental peaks at 876 and 877 cm^{-1} for DMA/goethite and DMA/hematite. The difference between experiment and theory for these is substantial, but may stem from the fact that there are not enough explicit waters in the first solvation shell for this rather complex system to properly mimic solvation and hydrogen bonding with DMA and the surface. The methods with higher basis sets with appropriate scaling factors do a much better job at representing these complexes. See the discussion in the Conclusions and Recommendations section for more on this topic.

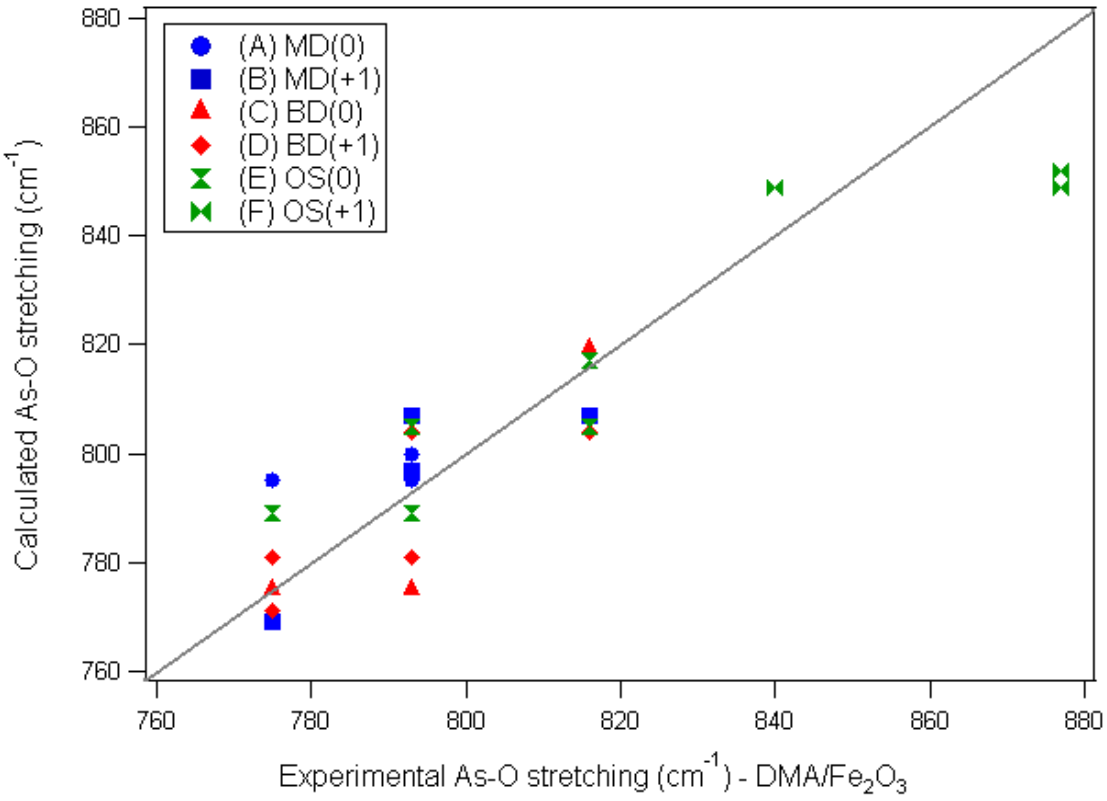

Figure 23: Correlation between experimental and calculated ν(As-O) using B3LYP/6-31G(d) with the IEFPCM solvation. The diagonal line shows the one-to-one line. Data for MD, BD and OS complexes is shown in Blue(circle, square), Red(triangle, rhombus) and Green(double triangles), respectively.

Also note that the outer-sphere Complex E does not have a protonated oxygen thus losing the As=O bond to form the resonance hybrid and hence showing frequencies of much lower wavenumber (e.g. 789 - 817 cm^{-1}). Note that a hybrid bond such as the one for Complex E can be thought of as a one and a half bond, instead of a single or a double bond. This can be seen from Table 1 when comparing DMA^- and DMA-H. The bonds for DMA-H are 1.67 Å for the As=O bond and 1.79 Å for As-OH bond, whereas for DMA^- the hybrid bonds are both 1.70 Å for both As-O bonds. This difference in the delocalized electrons also exists for Complexes E and F, as seen from Table 2, hence the difference in their vibrational frequencies.

Calculations also show the outer-sphere Complex F with ν(As-OH) frequencies at 749 cm^{-1} having a blue-shift of ~ 50 cm^{-1} when compared to DMA in the bulk. This has yet to be determined by experiment since the peaks were too low in intensity to be detected using DMA(aq) with a concentration of 0.001 M for the experiment shown in Figure 21.

4.4 Adsorption Thermodynamics of DMA on iron oxide clusters

Calculations that include Gibbs free energies of adsorption, ΔG_{ads}, can give insight into the type of reactions that are more thermodynamically favourable (i.e. having a more negative ΔG_{ads}) at the water/solid interface. Computationally, the Gibbs energy is calculated by adding the thermal correction to Gibbs free energy, G_{corr} (found in the Thermochemistry section of the Gaussian output file) to the electronic energy, E_0, as shown in Equation 4.2 below:

$$\text{Gibbs energy} = E_0 + G_{corr} \qquad \textbf{(Eqn. 4.2)}$$

Once, the Gibbs energies are calculated, various theoretical ligand exchange reactions can be built using the optimized structures a through e, in Figures 11 and 13, as the reactants and the optimized Complexes A through F, in Figures 14, 15 and 16, as the products. The difference between the Gibbs energies of the products and the Gibbs energies of the reactants will equal ΔG_{ads} as shown earlier in Equation 1.1.

The Gibbs energies for Structures a - e and Complexes A - F used for calculating ΔG_{ads} are shown in Table 7 for the B3LYP and BMK/6-311+G(d,p) level of theory with the IEFPCM solvation model. The electronic energies and thermal corrections are omitted for simplicity but are included in Appendix C.

Table 7: Gibbs energies (a.u.) of optimized DMA/iron oxide Complexes and Structures

Structures	Gibbs Energy (a.u.) B3LYP/6-311+G(d,p)	Gibbs Energy (a.u.) BMK/6-311+G(d,p)
a. DMA-H · $(H_2O)_4$	-2772.608493	-2771.153028
b. DMA^- · $(H_2O)_4$	-2772.163432	-2770.708347
c. DMA^- · $(H_2O)_6$	-2925.081810	-2923.535857
d. $Fe_2(OH)_6(OH_2)_2$ · $(H_2O)_6$	-3594.349649	-3592.626045
e. $Fe_2(OH)_5(OH2)_5^+$ · $(H_2O)_4$	-3594.783205	-3593.066558
Monodentate Complexes		
A. DMA-$Fe_2(OH)_5(OH_2)_3$ · $(H_2O)_5$	-5984.685433	-5981.736279
B. DMA-$Fe_2(OH)_4(OH_2)_5^+$ · $(H_2O)_4$	-5985.123731	-5982.173999
Bidentate Complexes		
C. DMA-$Fe_2(OH)_5(OH_2)_3$ · $(H_2O)_4$	-5908.224594	-5905.320755
D. DMA-$Fe_2(OH)_4(OH_2)_4^+$ · $(H_2O)_4$	-5908.671240	-5905.769926
Outer-Sphere Complexes		
E. DMA · $(H_2O)_5$ $Fe_2(OH)_5(OH_2)_4$	-6061.136813	-6058.139177
F. [DMA-H · $(H_2O)_4$ $Fe_2(OH)_5(OH_2)_5]^+$	-6061.566109	-6058.568499
Water Clusters - Leaving groups		
H_2O	-76.462870	-76.419793
OH^- · $(H_2O)_2$	-228.904940	-228.770376

The calculated Gibbs free energies of adsorption (ΔG_{ads}) for various hypothetical ligand exchange reactions are calculated using Equation 1.1 for two different cases. Since DMA has a $pK_a = 6.2$, the acidic environments with pH < 6.2 will have DMA-H as the dominant species, while in neutral and slightly basic environments with 6.2 < pH < 9, will have DMA^- as the dominant species. For both environments, the DMA species are considered to react with neutral and positively charged iron hydroxide clusters (structures d and e) to form neutral Complexes (A, C and E) and positively charged Complexes (B, D and F). The ligand exchange reactions are shown in Table 8 below with ΔG_{ads} for both the B3LYP and BMK/6-311+G(d,p) methods, with the latter represented in brackets ( ).

Table 8: Calculated ΔG_{ads} (kJ/mol) for ligand exchange reactions of DMA and iron oxides. Calculated using B3LYP/6-311+G(d,p) and BMK/6-311+G(d,p) with the IEFPCM solvation model.

Ligand Exchange Reactions for DMA and iron oxides	**ΔG_{ads} (kJ/mol)**
Simulated neutral and slightly basic environments (6.2 < pH < 9)	**B3LYP** (BMK)
yielding neutral complexes A, C and E	
1. $DMA^- \cdot(H_2O)_4 + Fe_2(OH)_5(OH_2)_5^+ \cdot(H_2O)_4 \rightarrow DMA\text{-}Fe_2(OH)_5(OH_2)_3 \cdot(H_2O)_5 + 5(H_2O)$	**-140** (-158)
2. $DMA^- \cdot(H_2O)_4 + Fe_2(OH)_5(OH_2)_5^+ \cdot(H_2O)_4 \rightarrow DMA\text{-}Fe_2(OH)_5(OH_2)_3 \cdot(H_2O)_4 + 6(H_2O)$	**-145** (-170)
3. $DMA^- \cdot(H_2O)_4 + Fe_2(OH)_5(OH_2)_5^+ \cdot(H_2O)_4 \rightarrow DMA \cdot(H_2O)_4\, Fe_2(OH)_5(OH_2)_4 + 5(H_2O)$	**-109** (-114)
yielding charged complexes B and D	
4. $DMA^- \cdot(H_2O)_4 + Fe_2(OH)_5(OH_2)_5^+ \cdot(H_2O)_4 \rightarrow DMA\text{-}Fe_2(OH)_4(OH_2)_5^+ \cdot(H_2O)_4 + OH^- \cdot(H_2O)_2 + 2(H_2O)$	**-20** (-24)
5. $DMA^- \cdot(H_2O)_4 + Fe_2(OH)_5(OH_2)_5^+ \cdot(H_2O)_4 \rightarrow DMA\text{-}Fe_2(OH)_4(OH_2)_4^+ \cdot(H_2O)_4 + OH^- \cdot(H_2O)_2 + 3(H_2O)$	**-48** (-65)
Simulated acidic environments (pH < 6.2)	
yielding neutral complexes A, C and E	
6. $DMA\text{-}H \cdot(H_2O)_4 + Fe_2(OH)_6(OH_2)_2 \cdot(H_2O)_6 \rightarrow DMA\text{-}Fe_2(OH)_5(OH_2)_3 \cdot(H_2O)_5 + 3(H_2O)$	**-109** (-147)
7. $DMA\text{-}H \cdot(H_2O)_4 + Fe_2(OH)_6(OH_2)_2 \cdot(H_2O)_6 \rightarrow DMA\text{-}Fe_2(OH)_5(OH_2)_3 \cdot(H_2O)_4 + 6(H_2O)$	**-115** (-159)
8. $DMA\text{-}H \cdot(H_2O)_4 + Fe_2(OH)_6(OH_2)_2 \cdot (H_2O)_6 \rightarrow DMA \cdot(H_2O)_5\, Fe_2(OH)_5(OH_2)_4 + 4(H_2O)$	**-79** (-103)
yielding charged complexes B, D and F	
9. $DMA\text{-}H \cdot(H_2O)_4 + Fe_2(OH)_5(OH_2)_5^+ \cdot(H_2O)_4 \rightarrow DMA\text{-}Fe_2(OH)_4(OH_2)_5^+ \cdot(H_2O)_4 + 5(H_2O)$	**-122** (140)
10. $DMA\text{-}H \cdot(H_2O)_4 + Fe_2(OH)_5(OH_2)_5^+ \cdot(H_2O)_4 \rightarrow DMA\text{-}Fe_2(OH)_4(OH_2)_4^+ \cdot(H_2O)_4 + 6(H_2O)$	**-149** (181)
11. $DMA\text{-}H \cdot(H_2O)_4 + Fe_2(OH)_5(OH_2)_5^+ \cdot(H_2O)_4 \rightarrow DMA\text{-}H \cdot(H_2O)_4\, Fe_2(OH)_5(OH_2)_5^+ + 4(H_2O)$	**-68** (74)

All of the calculations in Table 8 yield a negative ΔG_{ads}, thus indicating that they are all thermodynamically favourable. The most favourable reactions were those that formed the bidentate complexes in reactions 2, 5, 7 and 10 with the lowest negative values for ΔG_{ads}, followed by the monodentate reactions 1, 4, 6 and 9 and lastly the outer-sphere reactions 3, 8 and 11. There were only systematic differences between the B3LYP and BMK models, with the BMK model showing the same trend in thermodynamic favorability and with calculated ΔG_{ads} differences ranging from 5 - 44 kJ/mol between the two models.

Different hypothetical ligand exchange reactions need to be constructed when the SMD solvation model is used (compared to the ones in Table 8) because of the different geometries and change in coordination number for the iron complexes. See Appendix B for the optimized geometries of Structures a – e and Complexes A – F when the SMD solvation model is used for B3LYP/6-311+G(d,p) calculations. The electronic energies, thermal correction to Gibbs and the Gibbs energy (calculated using Equation 4.2) for the SMD structures and complexes are shown in Table 9 below.

As in Table 8, ligand exchange reactions were constructed for acidic environments with pH < 6.2 where the DMA molecule is mostly in the protonated form as well as neutral or slightly basic environments with 6.2 < pH < 9 where the DMA molecule is mostly in the deprotonated form. Various hypothetical ligand exchange reactions were constructed with the Structures and Complexes in Table 9 and the ΔG_{ads} of the adsorption reactions were calculated using Equation 1.1. The ligand exchange reactions are displayed in Table 10 below for the B3LYP/6-311+G(d,p) method with the SMD model of solvation.

Table 9: Gibbs energies of optimized DMA/iron oxide Complexes and Structures calculated using B3LYP/6-311+G(d,p) and SMD solvation model.

DMA structures	Electronic Energy (a.u.)	Thermal Correction to Gibbs	Gibbs Energy (a.u.)
a. DMA-H · $(H_2O)_4$	-2772.778568	0.140383	-2772.638185
b. DMA^- · $(H_2O)_4$	-2772.310287	0.120038	-2772.190249
c. DMA^- · $(H_2O)_6$	-2925.273099	0.165026	-2925.108073
Iron oxide structures			
d. $Fe_2(OH)_5(OH_2)_4^+$ ·$(H_2O)_5$	-3595.113708	0.219087	-3594.894621
e. $Fe_2(OH)_6(OH_2)$ ·$(H_2O)_7$	-3594.664969	0.199238	-3594.465731
Monodentate Complexes			
A. DMA-$Fe_2(OH)_5(OH_2)_2$ ·$(H_2O)_7$	-6138.013459	0.300252	-6137.713207
B. DMA-$Fe_2(OH)_4(OH_2)_3]^+$ ·$(H_2O)_6$	-5985.520958	0.276494	-5985.244464
Bidentate Complexes			
C. DMA-$Fe_2(OH)_5$ ·$(H_2O)_7$	-5908.600941	0.239602	-5908.361339
D. DMA-$Fe_2(OH)_4(OH_2)_2^+$ ·$(H_2O)_6$	-5909.048557	0.255667	-5908.792890
Outer-Sphere Complexes			
E. DMA ·$(H_2O)_7$ $Fe_2(OH)_5(OH_2)_2$	-6061.541655	0.282354	-6061.259301
F. DMA-H ·$(H_2O)_6$ $Fe_2(OH)_5(OH_2)_3^+$	-6061.994305	0.301904	-6061.692401
Water Clusters – Leaving groups			
H_2O	-76.471953	0.002703	-76.469250
OH^- ·$(H_2O)_2$	-228.945049	0.026154	-228.918895

The ligand exchange reactions for the SMD model of solvation in Table 10 show an even greater difference between the ΔG_{ads} values of the bidentate complexes and the rest, with the bidentate complexes in reactions 2, 5, 7 and 10 (Table 10) being the most thermodynamically favourable (lowest ΔG_{ads}).

Table 10: Calculated ΔG_{ads} (kJ/mol) for ligand exchange reactions of DMA and iron oxides. Calculated using B3LYP/6-311+G(d,p) and the SMD solvation model.

Ligand Exchange Reactions for DMA and iron oxides	**ΔG_{ads} (kJ/mol)***
Simulated neutral and slightly basic environments (6.2 < pH < 9)	
yielding neutral complexes A, C and E (from Appendix B)	
1. $DMA^- \cdot(H_2O)_4 + Fe_2(OH)_5(OH_2)_4^+ \cdot(H_2O)_5 \rightarrow DMA\text{-}Fe_2(OH)_5(OH_2)_2 \cdot(H_2O)_7 + 3(H_2O)$	**-95**
2. $DMA^- \cdot(H_2O)_4 + Fe_2(OH)_5(OH_2)_4^+ \cdot(H_2O)_5 \rightarrow DMA\text{-}Fe_2(OH)_5 \cdot(H_2O)_7 + 6(H_2O)$	**-241**
3. $DMA^- \cdot(H_2O)_4 + Fe_2(OH)_5(OH_2)_4^+ \cdot(H_2O)_5 \rightarrow DMA \cdot(H_2O)_7\ Fe_2(OH)_5(OH_2)_2 + 4(H_2O)$	**-135**
yielding charged complexes B and D (from Appendix B)	
4. $DMA^- \cdot(H_2O)_4 + Fe_2(OH)_5(OH_2)_4^+ \cdot(H_2O)_5 \rightarrow DMA\text{-}Fe_2(OH)_4(OH_2)_3^+ \cdot(H_2O)_6 + OH^- \cdot(H_2O)_2 + \cdot(H_2O)_2$	**-45**
5. $DMA^- \cdot(H_2O)_4 + Fe_2(OH)_5(OH_2)_4^+ \cdot(H_2O)_5 \rightarrow DMA\text{-}Fe_2(OH)_4(OH_2)_2^+ \cdot(H_2O)_6 + OH^- \cdot(H_2O)_2 + \cdot(H_2O)_3$	**-91**
Simulated acidic environments (pH < 6.2)	
yielding neutral complexes A, C and E (from Appendix B)	
6. $DMA\text{-}H \cdot(H_2O)_4 + Fe_2(OH)_6(OH_2) \cdot(H_2O)_7 \rightarrow DMA\text{-}Fe_2(OH)_5(OH_2)_2 \cdot(H_2O)_8 + 3(H_2O)$	**-45**
7. $DMA\text{-}H \cdot(H_2O)_4 + Fe_2(OH)_6(OH_2) \cdot(H_2O)_7 \rightarrow DMA\text{-}Fe_2(OH)_5 \cdot(H_2O)_7 + 6(H_2O)$	**-191**
8. $DMA\text{-}H \cdot(H_2O)_4 + Fe_2(OH)_6(OH_2) \cdot(H_2O)_7 \rightarrow DMA \cdot(H_2O)_7\ Fe_2(OH)_5(OH_2)_2 + 4(H_2O)$	**-85**
yielding charged complexes B, D and F (from Appendix B)	
9. $DMA\text{-}H \cdot(H_2O)_4 + Fe_2(OH)_5(OH_2)_4^+ \cdot(H_2O)_5 \rightarrow DMA\text{-}Fe_2(OH)_4(OH_2)_5^+ \cdot(H_2O)_4 + 5(H_2O)$	**-152**
10. $DMA\text{-}H \cdot(H_2O)_4 + Fe_2(OH)_5(OH_2)_4^+ \cdot(H_2O)_5 \rightarrow DMA\text{-}Fe_2(OH)_4(OH_2)_2^+ \cdot(H_2O)_6 + 6(H_2O)$	**-198**
11. $DMA\text{-}H \cdot(H_2O)_4 + Fe_2(OH)_5(OH_2)_4^+ \cdot(H_2O)_5 \rightarrow DMA\text{-}H \cdot(H_2O)_6\ Fe_2(OH)_5(OH_2)_3^+ + 4(H_2O)$	**-96**

Surprisingly, the calculations using the SMD model show outer-sphere complexes in reactions 3 and 8 being more thermodynamically favourable than their counterpart monodentate complexes in reactions 1 and 6 with a difference of 40 kJ/mol for ΔG_{ads} in both cases. This differs from the trend observed in the previous reactions of Table 8 when using the IEFPCM model. As an example, when comparing reactions 1 from Table 8 and Table 10, which form the monodentate neutral complex A, a difference in ΔG_{ads} of 45 kJ/mol between the IEFPCM and SMD solvation models is observed with the same B3LYP/6-311+G(d,p) method. Also when comparing reactions 3 from Table 8 and Table 10, which form the outer-sphere neutral complex E, a difference in ΔG_{ads} of 26 kJ/mol is observed. This suggests that

outer-sphere complexes may play a more important role in DMA complexation to iron oxides. This has also been observed in a recent surface complexation modeling study on the adsorption of DMA on iron-(oxyhydr)oxides, where the best fit to the DMA adsorption data was obtained using formation of these outer-sphere complexes.[43] From our computational results, this is not surprising both because outer-sphere complexation may be more thermodynamically favourable in some cases and also considering that the study was using the 840 cm^{-1} spectral component to quantify the surface coverage of DMA. Our calculations show clearly that the 840 cm^{-1} peak has contributions mostly from outer-sphere complexes but not from the bidentate complexes (see Figure 23 and the ν(As-O) for Complexes B and F in Table 6).

One possible explanation for the difference in energies between the calculations with the IEFPCM and SMD solvation models are their optimized geometries which differ considerably. Note the difference in the coordination geometry of the neutral outer-sphere Complex E shown in Figure 24 below for both the IEFPCM (left) and SMD (right) calculations.

Notice the 4-fold coordination geometry of the Fe atom in the SMD Complex and the 5-fold coordination geometry of the Fe atom in the IEFPCM Complex in Figure 24. These geometrical differences have an overall effect on the electronic energies which translates into differences in the Gibbs energies of the hypothetical ligand exchange reactions that are constructed.

It is also observed that, for all the reactions in Tables 8 and 10, the ones with the lowest ΔG_{ads} values (most negative) were generally the ones where electrostatics played a role (i.e. deprotonated DMA^- reacting with a positively charged surface). The types of leaving

groups also made a lot of difference when calculating ΔG_{ads} for the reactions. The reactions having just water molecules as leaving groups had a much lower ΔG_{ads} than the ones having OH^- and waters as leaving groups. This makes sense because waters are better leaving groups being more weakly bound to the iron and further away. Figure 25 shows the difference between H_2O and OH^- ligands bound to iron (iron oxide Surface d) with the Fe-OH distances, d(Fe-OH), ranging from 1.89 to 1.92 Å and the Fe-OH_2 distances, d(Fe-OH_2), ranging from 2.28 to 2.36 Å.

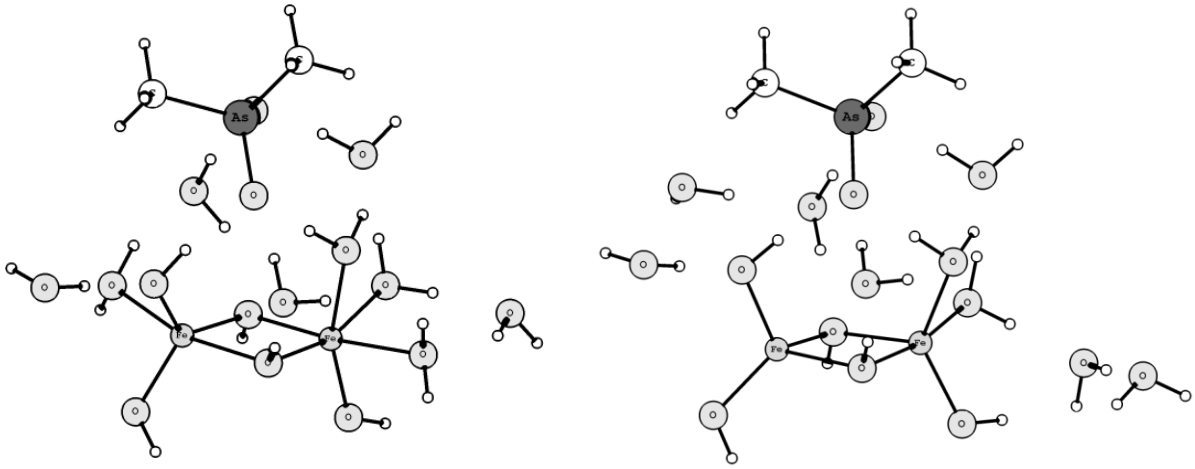

Complex E with **IEFPCM** Complex E with **SMD**

Figure 24: Optimized geometries of neutral outer-sphere Complex E using B3LYP/6-311+G(d,p)

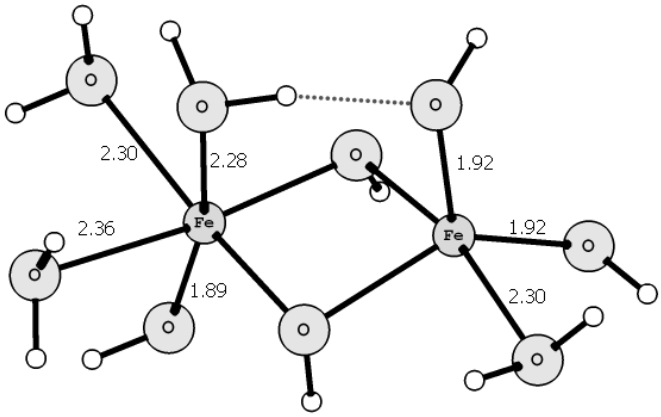

Figure 25: Iron oxide surface structure (Structure d) showing the Fe-OH and Fe-OH_2 distances in angstroms of the external ligands. Calculated using B3LYP/6-311+G(d,p) and the SMD solvation model.

All in all, thermodynamic data supports the conclusion that there is simultaneous formation of both inner- and outer-sphere complexes by showing that all complexation reactions in Table 8 and 10 are thermodynamically favourable with negative ΔG_{ads}. Bidentate complexation is the most favourable in all cases (having the most negative ΔG_{ads}), while monodentate complexation is calculated to be more favourable than outer-sphere when the IEFPCM solvation model is used. This order is reversed when the SMD solvation model is employed with the outer-sphere complexation having a more negative ΔG_{ads} than the monodentate, but still higher than the bidentate. Thus, favorability is predicted as bidentate > monodentate > outer-sphere by the B3LYP and BMK/6-311+G(d,p) models with IEFPCM solvation and bidentate > outer-sphere > monodentate by the B3LYP/6-311+G(d,p) model with SMD solvation.

4.5 Adsorption Thermodynamics of iAs(V) on iron oxide clusters

Calculations with inorganic As(V) were also performed to compare complexation energies with the organic DMA systems. Table 11 below contains the Gibbs energies (a.u.) for the Structures f, g (the arsenic acid species most important at environmental pH) and Complexes G, H used to construct ligand exchange reactions and calculate ΔG_{ads} for the inorganic arsenic system.

With the Structures f, g, and the iron oxide surface displayed in Table 11, four theoretical ligand exchange reactions can be constructed leading to the formation of inorganic Complexes G and H and the presented leaving groups. Since arsenic acid is a triprotic acid with pK_a values at 2.19, 6.94 and 11.5, the most important species present in

environmental conditions would be $H_2AsO_4^-$ and $HAsO_4^{2-}$. Therefore, hypothetical reactions are built for pH < 6.9 and pH > 6.9 and their calculated ΔG_{ads} values for the B3LYP and BMK/6-311+G(d,p) methods shown in Table 12, with the BMK method shown in brackets ( ).

Table 11: Gibbs energies of optimized inorganic As(V) Complexes and Structures

Inorganic As(V) Structures	Gibbs Energy (a.u.) B3LYP/6-311+G(d,p)	Gibbs Energy (a.u.) BMK/6-311+G(d,p)
f. $HAsO_4^{-2} \cdot (H_2O)_4$	-2843.622865	-2842.168587
g. $H_2AsO_4^- \cdot (H_2O)_4$	-2844.087200	-2842.633781
Iron oxide surface		
e. $Fe_2(OH)_5(OH2)_5^+ \cdot (H_2O)_4$	-3594.783205	-3593.066558
d. $Fe_2(OH)_6(OH_2)_2 \cdot (H_2O)_6$	-3594.349649	-3592.626045
Bidentate iAs(V) Complexes		
G. $HAsO_4\text{-}Fe_2(OH)_4(OH_2)_4 \cdot (H_2O)_4$	-5980.145907	-5977.245360
H. $H_2AsO_4\text{-}Fe_2(OH)_4(OH_2)_4^+ \cdot (H_2O)_4$	-5980.578493	-5977.681467
Water Clusters – Leaving groups		
H_2O	-76.462870	-76.419793
$OH^- \cdot (H_2O)_2$	-228.904940	-228.770376

From Table 12 below we observe that the most thermodynamically favourable reactions are 1 and 4 leading to formation of the neutral Complex G. When put side to side, the calculated ΔG_{ads} of reaction 1 is very similar with work done by Kubicki et al[44] on the inorganic As(V) system where they calculated a ΔG_{ads} = -140 kJ/mol for Equation 4.3.

$$H_2AsO_4^- \cdot (H_2O)_8 + Fe_2(OH)_5(OH_2)_5^+ \cdot (H_2O)_4 \rightarrow Fe_2(OH)_4(OH_2)_4\text{-}HAsO_4 \cdot (H_2O)_4 + 10(H_2O) \quad \textbf{(Eqn. 4.3)}$$

Note that the only difference between Reaction 1 (Table 12) and Equation 4.3 are the number of explicit waters surrounding the arsenic species and that this translates into a 2 kJ/mol difference in the ΔG_{ads} values. This comparison also justifies why using four explicit waters is sufficient.

Table 12: Calculated ΔG_{ads} (kJ/mol) for ligand exchange reactions of iAs(V) and iron oxides. Calculated using B3LYP/6-311+G(d,p) and BMK/6-311+G(d,p) with IEFPCM solvation.

Ligand exchange reactions for iAs(V) and iron oxide surfaces	**ΔG_{ads} (kJ/mol)**
Simulated slightly acidic environments (pH < 6.9)	**B3LYP** (BMK)
yielding complexes G and H	
1. $H_2AsO_4^- \cdot(H_2O)_4 + Fe_2(OH)_5(OH_2)_5^+ \cdot(H_2O)_4 \rightarrow Fe_2(OH)_4(OH_2)_4\text{-}HAsO_4 \cdot(H_2O)_4 + 6(H_2O)$	**-138** (-167)
2. $H_2AsO_4^- \cdot(H_2O)_4 + Fe_2(OH)_6(OH_2)_2 \cdot(H_2O)_6 \rightarrow Fe_2(OH)_4(OH_2)_4\text{-}HAsO_4 \cdot(H_2O)_4 + OH^- \cdot(H_2O)_2 + 3(H_2O)$	**-7** (-40)
3. $H_2AsO_4^- \cdot(H_2O)_4 + Fe_2(OH)_5(OH_2)_5^+ \cdot(H_2O)_4 \rightarrow Fe_2(OH)_4(OH_2)_4\text{-}H_2AsO_4^+ \cdot(H_2O)_4 + OH^- \cdot(H_2O)_2 + 3(H_2O)$	**-4** (-29)
Simulated neutral and slightly basic environments (pH > 6.9)	**B3LYP** (BMK)
yielding complex G	
4. $HAsO_4^{-2} \cdot(H_2O)_4 + Fe_2(OH)_5(OH_2)_5^+ \cdot(H_2O)_4 \rightarrow Fe_2(OH)_4(OH_2)_4\text{-}HAsO_4 \cdot(H_2O)_4 + OH^- \cdot(H_2O)_2 + 3(H_2O)$	**-88** (-105)

Reaction 1 in Table 12 is also comparable with organic reaction 2 in Table 8 where the neutral bidentate DMA Complex C forms, both yielding very similar results (a 7 kJ/mol difference when using the B3LYP method and only a 3 kJ/mol difference when using the BMK method). Similar to the reactions obtained for the organic DMA system, the difference in the two (B3LYP and BMK) methods is between 17 - 33 kJ/mol in the values of ΔG_{ads} and the reactions leading to OH^- and water as the leaving groups being less exothermic.

4.6 Desorption Thermodynamics of DMA

The study of desorption is particularly useful for designing technologies that look at removing pollutants from contaminated soils. In this study we want to see the effects that a strong desorbing agent, like phosphate, has on methylated arsenicals, such as DMA.

As seen throughout this thesis, not all DMA sorption is the same, with the stronger bound inner-sphere complexes (especially the bidentate complexes) being harder to remove from the Fe-hydroxides than the outer-sphere. This was shown in Figure 22, where the 775

cm^{-1} peak assigned to bidentate complexation lingers after 30 minutes of flushing with phosphate. It also was shown in a recent study that the amount of desorbed MMA and DMA decreases as the sorption residence time increases.[45] For example, the study found that after contaminating a particular soil sample with DMA and leaving it for 24 hours, 77% of the adsorbed DMA could be desorbed with a phosphate solution (made with 10X the initial concentration of DMA) and that after incubating the same sample for 6 months the desorption percentage dropped to 56%.

The dependence of DMA desorption on residence time may be explained in one of two ways or a possible combination of the two. Either arsenic speciation changes DMA into MMA or inorganic arsenic species that have stronger bonds to the soil, or alternatively, DMA itself forms stronger bonds over time (e.g. going from outer-sphere or monodentate to bidentate complexation). The last scenario is a good possibility and has support from the DFT calculations in this study since all DMA monodentate, bidentate and outer-sphere complexes have been shown to form simultaneously,[3] and all calculations show that ligand exchange reactions leading to the formation of bidentate complexes are the most thermodynamically favourable.

Moreover, analyzing the change in Gibbs energies (ΔG) for the reactions going from OS to MD, MD to BD and OS to BD shows that inter-complex reactions leading to the more strongly bound inner-sphere complexes are thermodynamically favourable with negative ΔG values between -5 and -81 kJ/mol for the B3LYP calculations and between -11 and -108 kJ/mol for the BMK calculations. The change in Gibbs free energies for the inter-complex reactions calculated using the optimized complexes A - F and their energies from Table 7 are

shown in Table 13 below for both the B3LYP and BMK methods, with the energies for the latter shown in brackets.

Table 13: Gibbs energies for inter-complex reactions

	ΔG (kJ/mol)
Outer-Sphere → Monodentate	**B3LYP** (BMK)
1. Complex E → Complex A + H_2O	**-30** (-44)
2. Complex F → Complex B + H_2O	**-54** (-66)
Monodentate → Bidentate	**B3LYP** (BMK)
3. Complex A → Complex C + H_2O	**-5** (-11)
4. Complex B → Complex D + H_2O	**-27** (-41)
Outer-Sphere → Bidentate	**B3LYP** (BMK)
5. Complex E → Complex C + 2(H_2O)	**-35** (-56)
6. Complex F → Complex D + 2(H_2O)	**-81** (-108)

The calculations in Table 13 show clearly that complexation favours the more strongly bound inner-sphere complexes, eventually converging toward the bidentate. This supports the idea that the drop in desorption for DMA after longer residence times may be due in part to DMA forming strongly bound complexes over time. This hypothesis could be confirmed by further experimental studies using surface sensitive techniques such as ATR-FTIR to follow the shift in the outer-sphere peaks over different incubation periods. It would follow that the peaks at 877 cm^{-1} and 840 cm^{-1} assigned solely to outer-sphere and monodentate complexes would get weaker over time as the peaks around 775 cm^{-1} assigned mostly to bidentate complexes would grow over time. The alternative hypothesis would be that in the presence of bacteria demethylation processes convert DMA into MMA and/or inorganic As over time which in turn form stronger bonds with the soil.

Phosphate structures and phosphate/Iron Oxide complexes were energy optimized using B3LYP/6-311+G(d,p) with the IEFPCM solvation model in order to study DMA

desorption by phosphate and construct ligand exchange reactions leading to the desorption of DMA and adsorption of phosphate. The optimized geometries of the phosphate structures are shown in Figure 26 below.

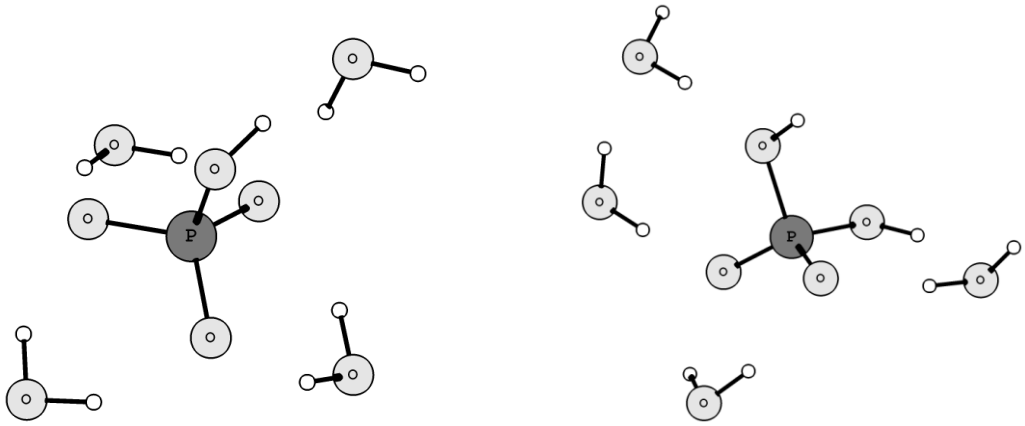

h. $HPO_4^{-2} \cdot (H_2O)_4$ **i.** $H_2PO_4^{-} \cdot (H_2O)_4$

Figure 26: The optimized geometries of phosphoric acid species HPO_4^{-2} and $H_2PO_4^{-}$ surrounded by four explicit waters. Calculated using B3LYP/6-311+G(d,p) and the IEFPCM solvation model.

The optimized geometries of the neutral and negatively charged complexes of phosphate and iron oxide are shown in Figure 27 below as complexes I and J.

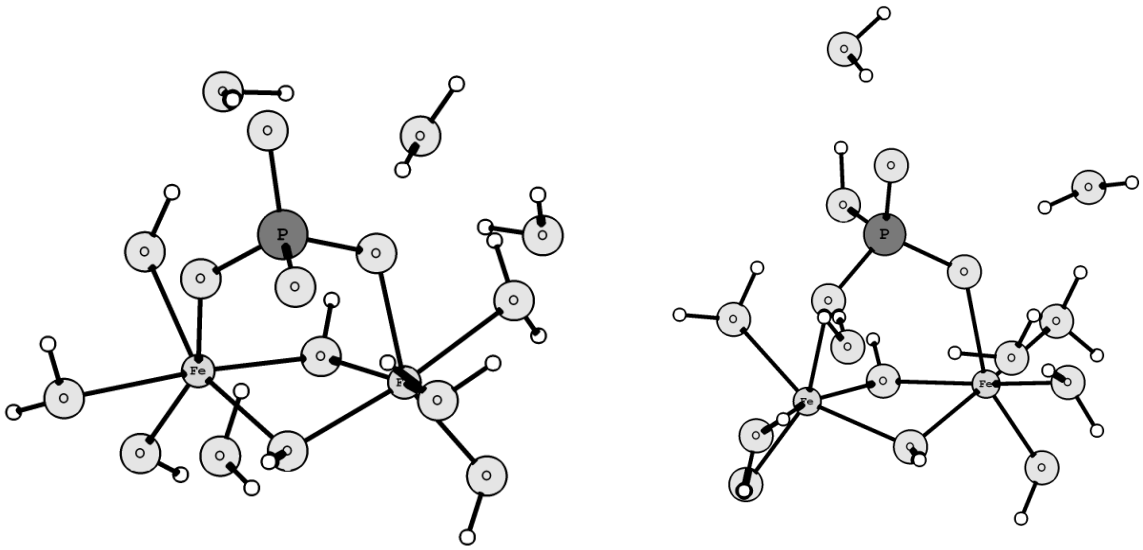

I. $Fe_2(OH)_4(OH_2)_4\text{-}PO_4^{-} \cdot (H_2O)_4$ **J.** $Fe_2(OH)_4(OH_2)_4\text{-}HPO_4 \cdot (H_2O)_4$

Figure 27: Optimized negatively charged (I) and neutral (J) phosphate complexes surrounded by water molecules. Calculated with B3LYP/6-311+G(d,p) and the IEFPCM solvation model.

The Structures in Figure 26 will be part of the reactants and the Complexes in Figure 27 will be the products of the desorption reactions. The Gibbs energies of the Structures and Complexes of all the reactants and products involved in the desorption reactions are shown in Table 14 below as calculated by the B3LYP/6-311+G(d,p) method and the IEFPCM solvation model.

The Gibbs energies in Table 14 have the thermal correction to Gibbs free energy (G_{corr}) added to them to construct the desorption reactions and calculations of ΔG_{des} (the change in the Gibbs free energy of desorption) as was done before using Equation 1.1 with ΔG_{des} replacing ΔG_{ads}. Table 15 shows desorption of monodentate DMA from the iron oxide surface using phosphate and the calculated ΔG_{des}. Since phosphoric acid has a $pK_{a2} = 7.2$, reactions with pH < 7.2 and pH > 7.2 will be considered separately with the proper phosphate species as the reactants in each of the two cases.

Table 14: Gibbs energies used in desorption reactions

Reactants	**Gibbs Energy (a.u.)**
h. $HPO_4^{-2} \cdot (H_2O)_4$	-949.218374
i. $H_2PO_4^{-} \cdot (H_2O)_4$	-949.675453
A. DMA-$Fe_2(OH)_5(OH_2)_3 \cdot (H_2O)_5$	-5984.685433
B. DMA-$Fe_2(OH)_4(OH_2)_5^{+} \cdot (H_2O)_4$	-5985.123731
C. DMA-$Fe_2(OH)_5(OH_2)_3 \cdot (H_2O)_4$	-5908.224594
D. DMA-$Fe_2(OH)_4(OH_2)_4^{+} \cdot (H_2O)_4$	-5908.671240
E. DMA $\cdot (H_2O)_5$ $Fe_2(OH)_5(OH_2)_4$	-6061.136813
F. $[DMAH \cdot (H_2O)_4$ $Fe_2(OH)_5(OH_2)_5]^{+}$	-6061.566109
Products	
a. $DMA^{-} \cdot (H_2O)_4$	-2772.608493
b. DMA-H $\cdot (H_2O)_4$	-2772.163432
I. $Fe_2(OH)_4(OH_2)_4$-$PO_4^{-} \cdot (H_2O)_4$	-4085.289723
J. $Fe_2(OH)_4(OH_2)_4$-$HPO_4 \cdot (H_2O)_4$	-4085.743183
Water – Leaving group	
H_2O	-76.462870

The reactions in Table 15 and their ΔG_{des} values indicate that desorption of monodentate DMA from iron oxides is thermodynamically favourable with negative ΔG_{des} throughout, ranging from -1 to -72 kJ/mol. According to the calculations, desorption seems to be more favourable in slightly basic conditions. This makes sense since the primary species of phosphate at that pH is HPO_4^{-2} leading to reactions where electrostatics plays a more important role (see Reaction 5 in Table 15).

Similarly, the ligand exchange reactions leading to desorption of bidentate DMA complexes by phosphate species relevant for environmental pH ranges and their calculated ΔG_{des} values are displayed in Table 16 below.

Table 15: Calculated ΔG_{des} values for desorption of **monodentate** DMA using phosphate

Ligand exchange reactions	**ΔG_{des} (kJ/mol)**
Simulated neutral and slightly acidic environments (pH < 7.2)	
desorption of neutral Complex A	
1. $H_2PO_4^- \cdot(H_2O)_4$ + DMA-$Fe_2(OH)_5(OH_2)_3 \cdot(H_2O)_5$ → $Fe_2(OH)_4(OH_2)_4$-$HPO_4 \cdot(H_2O)_4$ + $DMA^- \cdot(H_2O)_4$ + H_2O	**-23**
2. $H_2PO_4^- \cdot(H_2O)_4$ + DMA-$Fe_2(OH)_5(OH_2)_3 \cdot(H_2O)_5$ → $Fe_2(OH)_4(OH_2)_4$-$PO_4^- \cdot(H_2O)_4$ + DMA-H $\cdot(H_2O)_4$ + H_2O	**-1**
desorption of charged Complex B	
3. $H_2PO_4^- \cdot(H_2O)_4$ + DMA-$Fe_2(OH)_4(OH_2)_5^+ \cdot(H_2O)_4$→ $Fe_2(OH)_4(OH_2)_4$-$HPO_4 \cdot(H_2O)_4$ + DMA-H $\cdot(H_2O)_4$ + H_2O	**-40**
Simulated slightly basic environments (pH > 7.2)	
desorption of neutral Complex A	
4. $HPO_4^{-2} \cdot(H_2O)_4$ + DMA-$Fe_2(OH)_5(OH_2)_3 \cdot(H_2O)_5$ → $Fe_2(OH)_4(OH_2)_4$-$PO_4^- \cdot(H_2O)_4$ + $DMA^- \cdot(H_2O)_4$ + H_2O	**-32**
desorption of charged Complex B	
5. $HPO_4^{-2} \cdot(H_2O)_4$ + DMA-$Fe_2(OH)_4(OH_2)_5^+ \cdot(H_2O)_4$→ $Fe_2(OH)_4(OH_2)_4$-$HPO_4 \cdot(H_2O)_4$ + $DMA^- \cdot(H_2O)_4$ + H_2O	**-72**

The desorption reactions of bidentate DMA in Table 16 are also thermodynamically favourable but not as favourable as the monodentate desorption reactions with ΔG_{des} values ranging between -5 and -45 kJ/mol. As before, it is also observed that desorption of

bidentate complexes is favoured in the slightly basic environments, most likely due to electrostatics.

Table 16: Calculated ΔG_{des} values for desorption of **bidentate** DMA using phosphate

Ligand exchange reactions	**ΔG_{des} (kJ/mol)**
Simulated neutral and slightly acidic environments (pH < 7.2)	
desorption of neutral Complex C	
6. $H_2PO_4^- \cdot(H_2O)_4$ + DMA-$Fe_2(OH)_5(OH_2)_3 \cdot(H_2O)_4$ → $Fe_2(OH)_4(OH_2)_4$-$HPO_4 \cdot(H_2O)_4$ + $DMA^- \cdot(H_2O)_4$	**-17**
7. $H_2PO_4^- \cdot(H_2O)_4$ + DMA-$Fe_2(OH)_5(OH_2)_3 \cdot(H_2O)_4$ → $Fe_2(OH)_4(OH_2)_4$-$PO_4^- \cdot(H_2O)_4$ + DMA-H $\cdot(H_2O)_4$	**-5**
desorption of charged Complex D	
8. $H_2PO_4^- \cdot(H_2O)_4$ + DMA-$Fe_2(OH)_4(OH_2)_4^+ \cdot(H_2O)_4$ → $Fe_2(OH)_4(OH_2)_4$-$HPO_4 \cdot(H_2O)_4$ + DMA-H $\cdot(H_2O)_4$	**-13**
Simulated slightly basic environments (pH > 7.2)	
desorption of neutral Complex C	
9. $HPO_4^{-2} \cdot(H_2O)_4$ + DMA-$Fe_2(OH)_5(OH_2)_3 \cdot(H_2O)_4$ → $Fe_2(OH)_4(OH_2)_4$-$PO_4^- \cdot(H_2O)_4$ + $DMA^- \cdot(H_2O)_4$	**-27**
desorption of charged Complex D	
10. $HPO_4^{-2} \cdot(H_2O)_4$ + DMA-$Fe_2(OH)_4(OH_2)_4^+ \cdot(H_2O)_4$ → $Fe_2(OH)_4(OH_2)_4$-$HPO_4 \cdot(H_2O)_4$ + $DMA^- \cdot(H_2O)_4$	**-45**

The ligand exchange reactions leading to desorption of outer-sphere DMA complexes by phosphate species relevant for environmental pH and their calculated ΔG_{des} values are displayed in Table 17 below.

The desorption reactions for outer-sphere DMA in Table 17 are the most thermodynamically favourable with ΔG_{des} values ranging between -31 and -126 kJ/mol. As it was with the monodentate and bidentate reactions it is also observed that the reactions are more thermodynamically favourable under slightly basic environments.

Table 17: Calculated ΔG_{des} values for desorption of **outer-sphere** DMA using phosphate

Ligand exchange reactions	**ΔG_{des} (kJ/mol)**
Simulated neutral and slightly acidic environments (pH < 7.2)	
desorption of neutral Complex E	
11. $H_2PO_4^- \cdot(H_2O)_4$ + DMA $\cdot(H_2O)_5$ $Fe_2(OH)_5(OH_2)_4 \rightarrow$ $Fe_2(OH)_4(OH_2)_4$-$HPO_4 \cdot(H_2O)_4$ + $DMA^- \cdot(H_2O)_4$ + $2(H_2O)$	**-53**
12. $H_2PO_4^- \cdot(H_2O)_4$ + DMA $\cdot(H_2O)_5$ $Fe_2(OH)_5(OH_2)_4 \rightarrow$ $Fe_2(OH)_4(OH_2)_4$-$PO_4^- \cdot(H_2O)_4$ + DMA-H $\cdot(H_2O)_4$ + $2(H_2O)$	**-31**
desorption of charged Complex F	
13. $H_2PO_4^- \cdot(H_2O)_4$ + DMA-H $\cdot(H_2O)_5$ $Fe_2(OH)_5(OH_2)_5^+ \rightarrow$ $Fe_2(OH)_4(OH_2)_4$-$HPO_4 \cdot(H_2O)_4$ + DMA-H $\cdot(H_2O)_4$ + $2(H_2O)$	**-94**
Simulated slightly basic environments (pH > 7.2)	
desorption of neutral Complex E	
14. $HPO_4^{-2} \cdot(H_2O)_4$ + DMA $\cdot(H_2O)_5$ $Fe_2(OH)_5(OH_2)_4 \rightarrow$ $Fe_2(OH)_4(OH_2)_4$-$PO_4^- \cdot(H_2O)_4$ + $DMA^- \cdot(H_2O)_4$ + $2(H_2O)$	**-62**
desorption of charged Complex F	
15. $HPO_4^{-2} \cdot(H_2O)_4$ + DMA-H $\cdot(H_2O)_5$ $Fe_2(OH)_5(OH_2)_5^+ \rightarrow$ $Fe_2(OH)_4(OH_2)_4$-$HPO_4 \cdot(H_2O)_4$ + $DMA^- \cdot(H_2O)_4$ + $2(H_2O)$	**-126**

From the analysis of desorption reactions in Table 15, 16 and 17 we can conclude that desorption favorability increases in the order bidentate < monodentate < outer-sphere.

4.7 Transition States and Activation Barriers

Table 13 shows the type of inter-complex reactions that are thermodynamically favourable and driving the reactions forward but activation barriers (or activation energies) are not addressed. The activation energy, E_a, is the minimum energy required to start a reaction that goes from reactants to products with the activation energy being the potential barrier between two minima on the potential energy surface. [46]

The transition state is the configuration (or geometry) with the highest energy along the reaction path. Finding the energy of the transition state geometry using DFT calculations can help us get an idea about activation barriers as well as kinetics once the Gibbs energy of

activation, $\Delta G^{\ddagger}$, is calculated. The relationship between $\Delta G^{\ddagger}$ and the rate constant k is shown in Equation 2.4 below.[47]

$$k = \frac{k_B T}{h} \exp\left(-\frac{\Delta G^{\ddagger}}{RT}\right) \qquad \textbf{(Eqn. 4.4)}$$

Where k_B is the Boltzmann constant, h is the Planck constant, R is the gas constant and T is the temperature. The path of a hypothetical inter-complex reaction (transitioning from the monodentate to the bidentate complex) is shown in Figure 28 below with $\Delta G^{\ddagger}$ and a possible transition state structure.

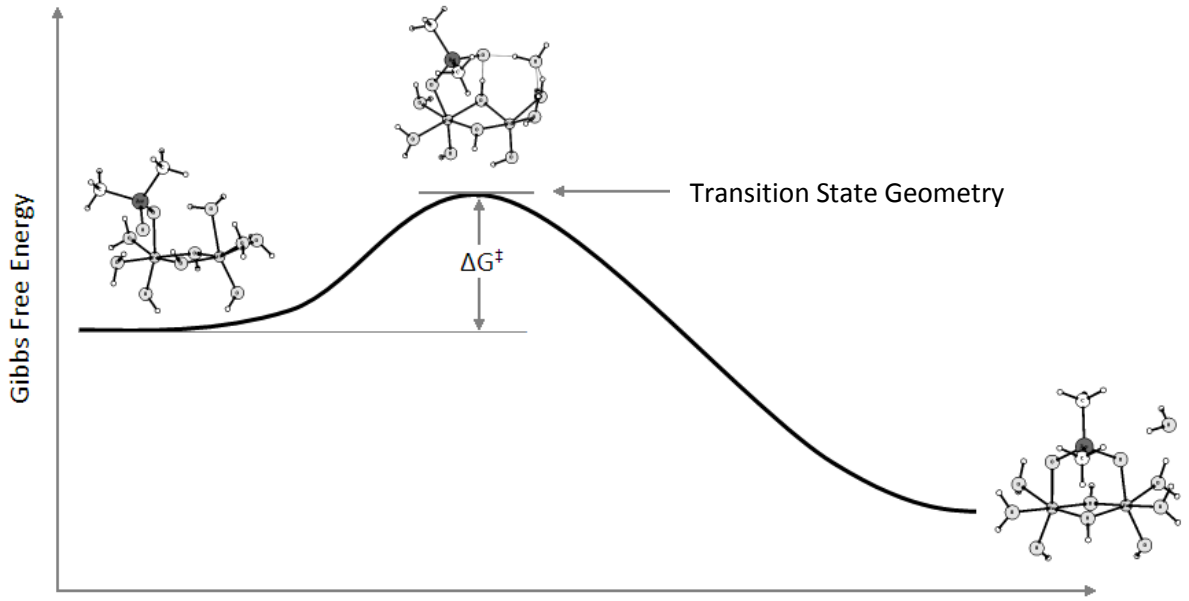

Figure 28: Reaction path showing the Gibbs free energy of activation between a MD and BD complex.

The geometry of a possible transition structure between monodentate Complex B and bidentate Complex D is shown in Figure 29 below and was calculated using B3LYP/6-31G(d) in the gas phase.

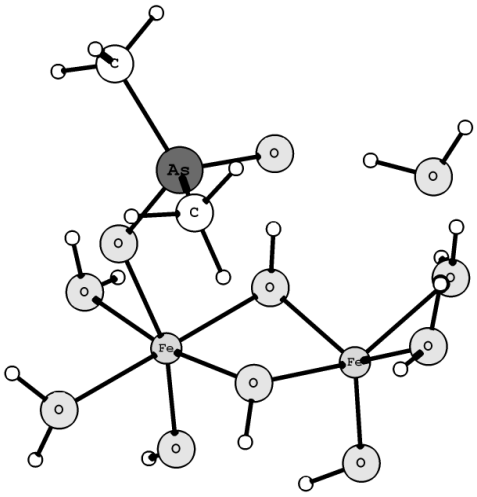

Figure 29: Possible transition structure between Complex B and D. Calculated with B3LYP/6-31G(d).

Because of the nature of the monodentate DMA/iron oxide complex with its rotational and bending freedom, locating a possible transition state between the monodentate and bidentate structures is a very challenging task. It becomes obvious that there are many local minima on the potential energy surface for the MD complexes and using the TS method in Gaussian is inadequate. Instead of finding the saddle point between the monodentate and bidentate structure, the TS method simply finds the saddle points between two different MD structures. This can be further understood using a simple explanation and Hammond's postulate[48] which asserts that for an exothermic reaction (such as the reaction between MD and BD), the transition state would resemble the reactant because it is closer to it in free energy. In our case the reactant is the monodentate structure and so the TS method is much more likely to find the saddle point between two adjacent local minima for MD complexes than to find the transition state between the MD and BD structures. A more advanced method for finding transition states, as well as a good guess to how the transition state might look like are therefore needed in this case.

The discovery of several possible MD conformations may explain the width of the peaks in the adsorption experiment shown in Figure 21, indicating that there may be formation of MD complexes of different varieties with various absorption peaks. It is also possible that if the activation barriers between the different MD complexes are small enough there are potential oscillations between the various forms at standard temperature and pressure conditions. Figure 30 below shows a few of the possible MD conformations that are stable and their electronic energies in atomic units.

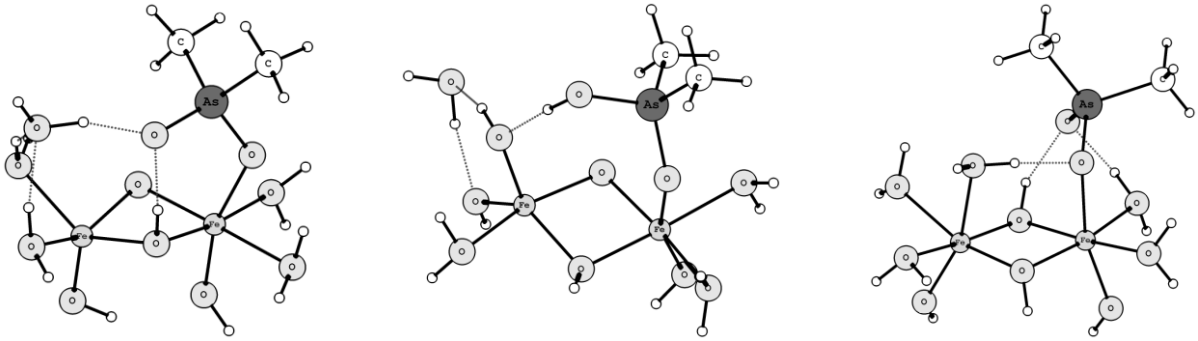

Complex B_1 (-5676.72010379 a.u.)

Complex B_2 (-5676.73029471 a.u.)

Complex B_3 (-5676.71233231 a.u.)

Figure 30: Three different monodentate conformations of Complex B and their electronic energies. Calculated using B3LYP/6-31G(d) in the gas phase.

More complexity is added to this when we consider that both outer-sphere and monodentate complexes absorb energy between 790 and 840 cm^{-1} and with their freedom of rotation, forming/breaking of hydrogen bonds and various proximities to the Fe atoms, can lead to monodentate and outer-sphere Complexes having a variety of ν(As-O) absorption frequencies. As a corollary to this, we expect that bidentate complexes with more constraints on their geometries would absorb IR light in a more narrow range. This seems to be the case when we analyze peaks around the 770 cm^{-1} region which, according to the

calculations, is a signature of bidentate complexes (note the 775 cm^{-1} peak in Figure 21). These predictions seem to be confirmed when taking a look at the B3LYP/6-311+G(d,p) data with the IEFPCM solvation model in Figure 32, which shows how scattered outer-sphere and monodentate peaks are when compared to the more constraint bidentate peaks.

The energies of the various MD complexes seen in Figure 30, BD complexes and possible transition state (TS) complexes are shown in Table 18 below with all calculations performed using B3LYP/6-31G(d) in the gas phase.

Table 18: Electronic and Gibbs free energies for various MD, BD and TS complexes. Calculated using B3LYP/6-31G(d) in the gas phase.

MD Species	Energy (a.u.)	Gibbs Energy (a.u.)
Complex B_1	-5676.720104	-5676.513207
Complex B_2	-5676.730295	-5676.528254
Complex B_3	-5676.712332	-5676.507638
BD Species		
Complex D_1	-5676.738532	-5676.532019
Transitions Structures		
TS 1	-5676.718765	-5676.511075
TS 2	-5676.716942	-5676.517069

According to the calculations above, the potential energy surface may look more like the one shown in Figure 31 below rather than the hypothetical one in Figure 28.

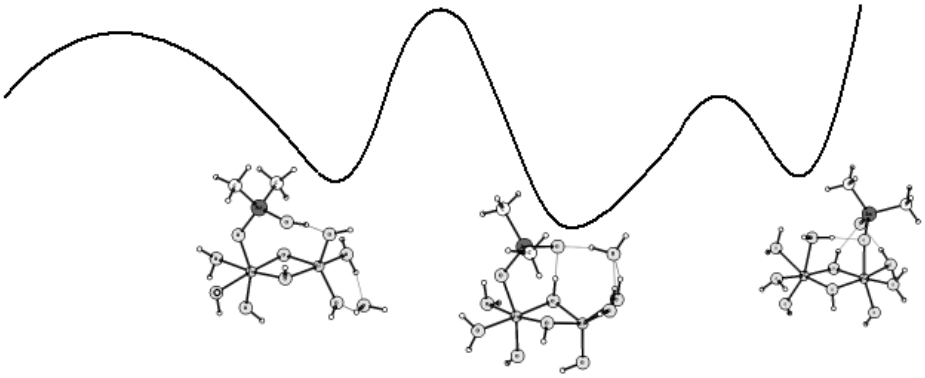

Figure 31: A more probable energy surface showing optimized MD structures and transition states.

5 Environmental Significance

The DFT calculations in this thesis accompanied by experimental results using ATR-FTIR have identified the different types of DMA/iron oxide complexes that form simultaneously in neutral, slightly basic and slightly acidic conditions, and they include the inner-sphere monodentate, bidentate and outer-sphere complexes analyzed in this study. The calculations in this study also show that formation of inner-sphere bidentate complexes are the most thermodynamically favourable and that hypothetical reactions going from outer-sphere and monodentate complexes toward the bidentate forms are also exothermic. This has implications concerning the mobility of DMA and its partitioning between the aqueous and solid phases that contain iron oxides. Iron rich soils would trap DMA by adsorbing it while iron poor soils would allow the arsenic to be more readily bio-available (being taken up by plants) and more mobile, with the potential of contaminating nearby water supplies. It is also hypothesized that adsorbed DMA on iron rich soils would change over time with the less strongly bound outer-sphere and monodentate complexes being replaced by the more strongly bound bidentate complexes.

The calculations of infrared spectra are valuable when interpreting experimental IR data and it was shown they are important in the assignment of peaks that are experimentally observed. For example, the adsorption peak at 840 cm^{-1} has been shown to belong mostly to the outer-sphere complexes. This idea has recently been used when constructing surface complexation models (SCMs) of DMA adsorption, where outer-sphere ligand exchange reactions gave the best fit for the data.[43] DFT calculations from this study can also be used to improve SCMs, which have great potential to become predictive in nature and be applied to

many different sites and different soil types. SCMs can potentially be used in "what-if" scenarios to answer environmental questions about how fast a pollutant plume can spread in the environment for the different types of soils that are present in a particular region.

Desorption studies show that in the presence of phosphate DMA desorption is thermodynamically favourable, which leads to the conclusion that in the presence of phosphate, DMA will become mobilized and therefore bio-available. The calculations predict that desorption favorability increases from bidentate to monodentate to outer-sphere, therefore lower concentrations of phosphate may only be able to mobilize the outer-sphere complexes, while higher concentrations of phosphate can mobilize even the more strongly bound inner-sphere complexes.

From a remediation point of view, these calculations support the idea that iron oxides can be used in technologies aimed at removing DMA. For example, data from this work and other experiments was used to propose the implementation of a method to reduce the arsenic content of organic rich fuels by washing fuels with slurries of Fe-(oxyhdr)oxides, instead of water alone and collecting contaminated particles for recycling.[3]

6 Conclusions and Recommendations

The computational studies of DMA adsorption in this thesis have been the first to analyze organic forms of arsenic interacting with iron oxides. DFT calculations accompanied by experimental ATR-FTIR results have identified the different types of DMA/iron oxide complexes that form simultaneously in neutral, slightly basic and slightly acidic conditions, and include the inner-sphere monodentate complexes A, B with d(As-Fe) within 3.4 - 4.9 Å, bidentate complexes C, D with d(As-Fe) within 3.3 - 3.4 Å and outer-sphere complexes E, F with d(As-Fe) 4.8 - 6.8 Å.

Various ligand exchange reactions were constructed to investigate the thermodynamics of inner- and outer-sphere complex formation and results indicated that both inner- and outer-sphere complex formation is thermodynamically favourable with bidentate complexes being most favourable. Similarly, desorption reactions of DMA due to interactions with phosphate ions determined that desorption favourability of DMA increases in the order of bidentate < monodentate < outer-sphere.

Calculated frequencies, ν(As-O), need to be corrected for anharmonicity (since chemical bonds deviate from harmonic behaviour) via multiplication by a scaling factor (F). The scaling factors used in this study were approximate scaling factors used in other studies and hence don't reflect the complexity of our system with our method, basis set and choice of solvation models. Therefore, more adequate scaling factors can be are derived by minimizing the sum of the residuals separating the theoretical (T_i) and experimental (E_i) frequencies. For this study the DMA on hematite system,[3] was chosen as the proper experimental candidate for the calibration of frequencies in our calculated DMA-iron oxide

clusters. The formula used in the calculation of the scaling factors is shown Equation 6.1 below where the residual R_i is minimized:

$$\min \sum R_i \quad \text{where} \quad R_i(F) = \left| T_i \cdot F - E_i \right| \qquad \textbf{(Eqn. 6.1)}$$

Equation 6.1 is a set of absolute value functions R with variable F of the form "y = mx + b" with constants m=T_i for the slope and b=-E_i for the y-intercept. Since these are absolute value functions, the range will always be positive with

$$R_i(F) = \begin{cases} T_i F - E_i & \text{if } T_i F - E_i \geq 0 \\ -(T_i F - E_i) & \text{if } T_i F - E_i < 0 \end{cases}$$

where the small "i" stands for the experimental ν(As-O) frequency (of DMA/hematite) for which the residual is calculated (i.e. $R_1(F)$ for 775 cm^{-1}, $R_2(F)$ for 793 cm^{-1}, etc.). The sum of the residuals is then minimized with respect to the scaling factor F. An example of this is shown in Appendix E.

Since scaling factors are method specific,[49] they were calculated separately (using Eqn. 6.1) for each of the four methods considered in this study, as shown in Table 19 below.

Table 19: Suitable frequency scale factors for various methods

Method	Scaling Factor (F)
B3LYP/6-31G(d) with IEFPCM	**0.9580**
B3LYP/6-311+G(d,p) with IEFPCM	**1.0307**
B3LYP/6-311+G(d,p) with SMD	1.0459
BMK/6-311+G(d,p) with IEFPCM	0.9851

Table 19 shows that a scaling factor that reduces the frequencies by approximately 4% is adequate when using the B3LYP/6-31G(d) but different scaling factors are needed for the more advanced methods when using arsenic and iron oxides. In particular, when using the

B3LYP method with the higher basis set 6-311+G(d,p) and the same IEFPCM solvation model, the scaling factor should be adjusted from reducing frequencies by 4% to increasing frequencies by 3% (i.e. F=1.0307 as seen in Table 19). Figure 32 shows how the correction factor for B3LYP/6-311+G(d,p) adjusts the frequencies to match with the peaks observed experimentally.

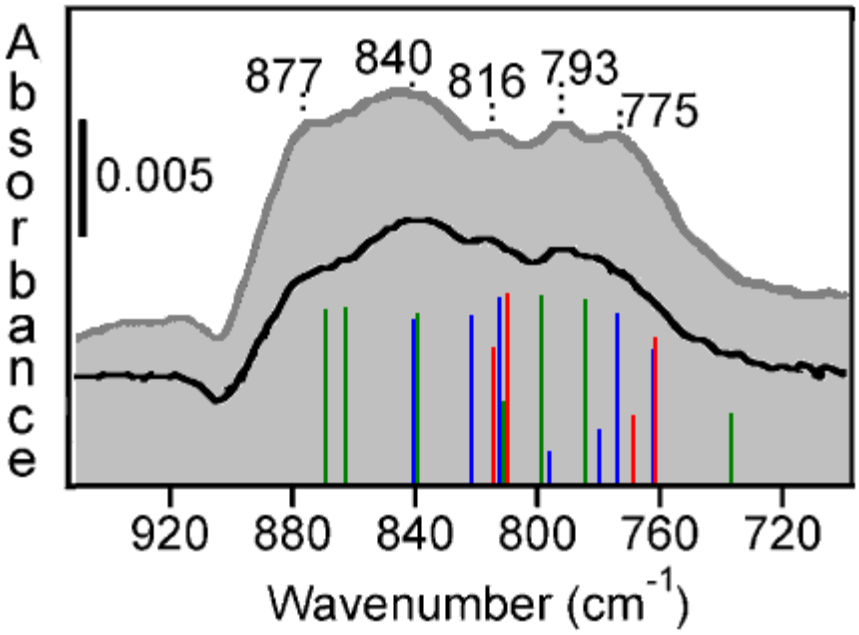

Figure 32: The ATR-FTIR adsorption spectra of DMA/hematite together with corrected frequencies using B3LYP/6-311+G(d,p) with IEFPCM. Line colors are blue for MD, red for BD and green for OS. Experimental data was reproduced from *Environ. Sci. Technol.*, 2010, *44* (20), pp 7802–7807 (see figures in Reference 3).

The B3LYP/6-311+G(d,p) method with the IEFPCM solvation model also shows monodentate peaks may be more scattered than predicted by the B3LYP/6-31G(d) method. In particular, from Figure 32 we can see that the peak at 840 cm^{-1} is shared by both outer-sphere (green) and monodentate (blue) complexes. Correcting frequencies for anharmonicity with the newly calculated scaling factors yield the following ν(As-O) stretching vibrations shown in Table 20.

Table 20: Calculated ν(As-O) frequencies (cm^{-1}) for Complexes A - F with the new scaling factors calculated in Table 19.

Complex	B3LYP 6-31G(d) IEFPCM	B3LYP 6-311+G(d,p) IEFPCM	B3LYP 6-311+G(d,p) SMD	BMK 6-311+G(d,p) IEFPCM
MD Complex A	793	777	754	788
Charge 0	798	825	815	815
MD Complex B	767	763	769	768
Charge +1	795	795	838	783
	806	815	853	816
		840		837
BD Complex C	773	762	775	786
Charge 0	817	816	813	819
BD Complex D	769	770	771	744
Charge +1	780	810	795	801
	802			821
OS Complex E	787	787	780	794
Charge 0	804	797	798	806
	815	812	806	841
		814	819	
OS Complex F	747	736	715	739
Charge +1	847	840	823	850
	850	864	868	
		870		

In conclusion, the B3LYP/6-311+G(d,p) method with the IEFPCM solvation model is a robust method to use, as seen from the calculations performed in this study, giving us the best results when compared to experiment. It is thus the DFT method of choice when performing calculations on arsenic and iron-oxide complexes. In addition, when doing vibrational frequency analysis of organoarsenicals and iron oxide clusters, this thesis recommends correcting calculated frequencies with a scaling factor of 1.0307 when using the B3LYP/6-311+G(d,p) method with the IEFPCM solvation model, to get results that agree best with experiment.

Appendix A: A study about the effects of adding explicit waters around **DMA** and **DMA/iron oxide** clusters. Calculations performed using **B3LYP/6-311+G(d,p)** with **IEFPCM** solvation model.

Table A1: The ν(As-O) frequencies of DMA^- with different number of explicit waters

Molecule	ν(As-O) frequencies (cm^{-1})	ν(As-O) with F=1.0416 (cm^{-1})
DMA^-	793, 812	826, 846
$DMA^- \cdot (H_2O)$	785, 795	818, 828
$DMA^- \cdot (H_2O)_2$	793, 806	826, 840
$DMA^- \cdot (H_2O)_3$	784, 808	817, 842
$DMA^- \cdot (H_2O)_4$	**787, 788**	**820, 821**
$DMA^- \cdot (H_2O)_5$	759, 788, 799	791*, 821, 832
$DMA^- \cdot (H_2O)_6$	**757, 788, 798**	**788*, 821, 831**
$DMA^- \cdot (H_2O)_7$	757, 781, 792	788*, 813, 825
$DMA^- \cdot (H_2O)_8$	779, 788	811, 821

* peaks form when strong H-bonds are present.

Table A2: Effects of explicit waters on the geometry of DMA^- with distances in Å.

	As-O_1	As-O_2	As-C_1	As-C_2
DMA^-	1.69	1.69	1.96	1.96
$DMA^- \cdot (H_2O)$	1.70	1.70	1.95	1.95
$DMA^- \cdot (H_2O)_2$	1.69	1.70	1.95	1.95
$DMA^- \cdot (H_2O)_3$	1.70	1.69	1.95	1.95
$DMA^- \cdot (H_2O)_4$	**1.70**	**1.70**	**1.94**	**1.94**
$DMA^- \cdot (H_2O)_5$	1.70	1.71	1.94	1.94
$DMA^- \cdot (H_2O)_6$	**1.71**	**1.71**	**1.94**	**1.94**
$DMA^- \cdot (H_2O)_7$	1.71	1.71	1.94	1.94
$DMA^- \cdot (H_2O)_8$	1.71	1.71	1.94	1.94

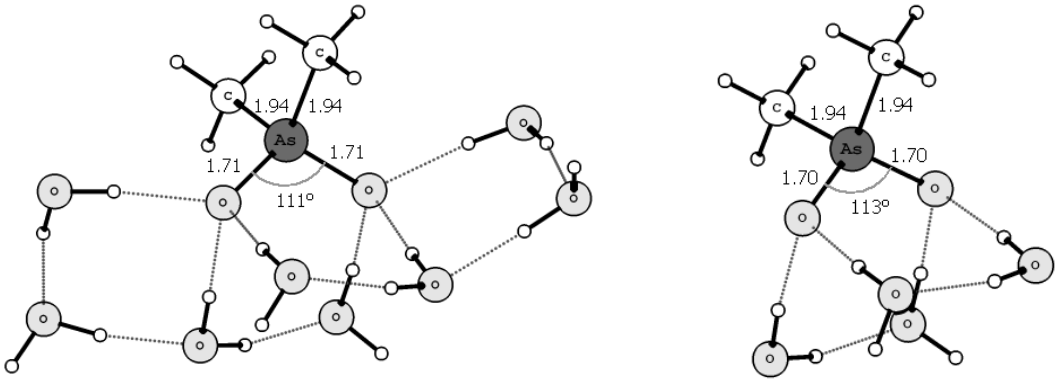

$DMA^- \cdot (H_2O)_8$ **$DMA^- \cdot (H_2O)_4$**

Figure A1: The effects of adding more explicit waters on the geometry of DMA^-. The differences are only minor between 4 and 8 explicit waters with Δd(As-O) = 0.004Å and Δa(O-As-O) = 2°.

Table A3: The As-O vibrational frequencies of DMA-H with different number of waters

Molecule	ν(As-O) frequencies (cm^{-1})	ν(As-O) with F=1.0416 (cm^{-1})
DMA-H	687, 961	716, 1001
DMA-H · (H_2O)	648, 850	675, 885
DMA-H · $(H_2O)_2$	661, 839	688, 874
DMA-H · $(H_2O)_3$	682, 843, 845	710, 878, 880
DMA-H · $(H_2O)_4$	**668, 849**	**696, 884**
DMA-H · $(H_2O)_5$	673, 836	701, 871
DMA-H · $(H_2O)_6$	660, 683, 823	687, 711, 857
DMA-H · $(H_2O)_7$	672, 825	700, 859
DMA-H · $(H_2O)_8$	660, 666, 827	687, 694, 861

Table A4: Effects of explicit waters on the geometry of DMA-H with distances in Å.

	As-O	As-OH	As-C_1	As-C_2
DMA-H	1.65	1.79	1.92	1.92
DMA-H · (H_2O)	1.67	1.79	1.93	1.93
DMA-H · $(H_2O)_2$	1.68	1.78	1.93	1.93
DMA-H · $(H_2O)_3$	1.68	1.77	1.93	1.92
DMA-H · $(H_2O)_4$	**1.67**	**1.79**	**1.93**	**1.93**
DMA-H · $(H_2O)_5$	1.68	1.78	1.93	1.92
DMA-H · $(H_2O)_6$	1.69	1.78	1.93	1.92
DMA-H · $(H_2O)_7$	1.69	1.78	1.93	1.92
DMA-H · $(H_2O)_8$	1.68	1.78	1.93	1.92

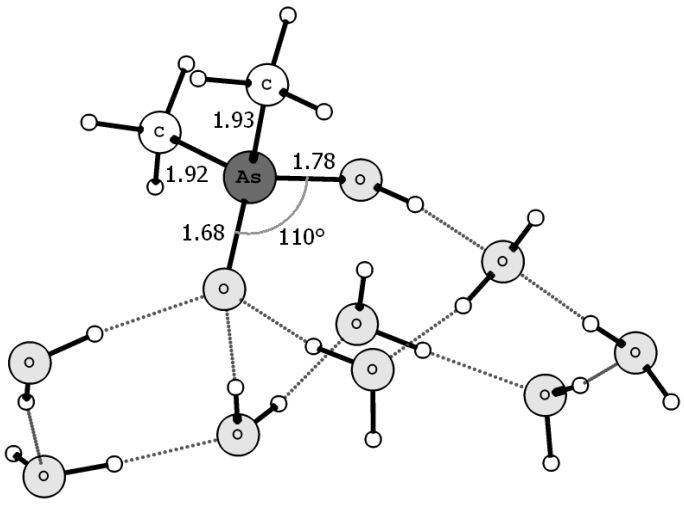

DMA-H · $(H_2O)_8$

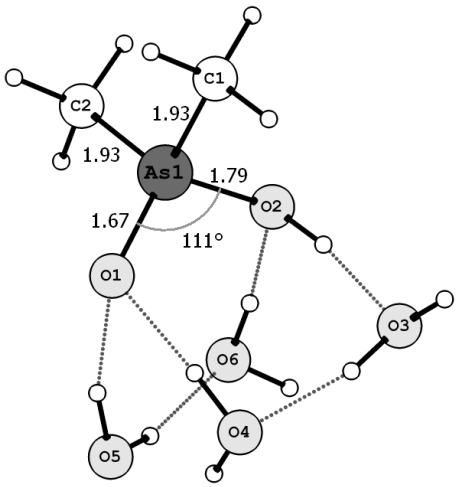

DMA-H · $(H_2O)_4$

Figure A2: The effects of adding more explicit waters on the geometry of DMA-H. The differences are only minor between 4 and 8 explicit waters with Δd(As-O) = 0.01Å and Δa(O-As-O) = 1°.

Table A5: The ν(As-O) frequencies of Complex D with different number of explicit waters

Molecule	ν(As-O) frequencies (cm^{-1})	ν(As-O) with F=1.0307 (cm^{-1})
Complex D	785, 804	809, 829
Complex D · (H_2O)	772, 804	796, 829
Complex D · $(H_2O)_2$	772, 791	796, 815
Complex D · $(H_2O)_3$	739, 780, 795	762, 804, 819
Complex D · $(H_2O)_4$	**747, 786**	**770, 810**
Complex D · $(H_2O)_5$	747, 785	770, 809
Complex D · $(H_2O)_6$	704, 750, 790	726, 773, 814

Table A6: Effects of explicit waters on the geometry of Complex D with distances in Å.

	As-O_1	As-O_2	As-Fe_1	As-Fe_2
Complex D	1.71	1.71	3.30	3.30
Complex D · (H_2O)	1.71	1.72	3.30	3.33
Complex D · $(H_2O)_2$	1.72	1.72	3.33	3.33
Complex D · $(H_2O)_3$	1.72	1.72	3.31	3.33
Complex D · $(H_2O)_4$	**1.73**	**1.72**	**3.39**	**3.30**
Complex D · $(H_2O)_5$	1.73	1.72	3.39	3.30
Complex D · $(H_2O)_6$	1.73	1.72	3.37	3.31

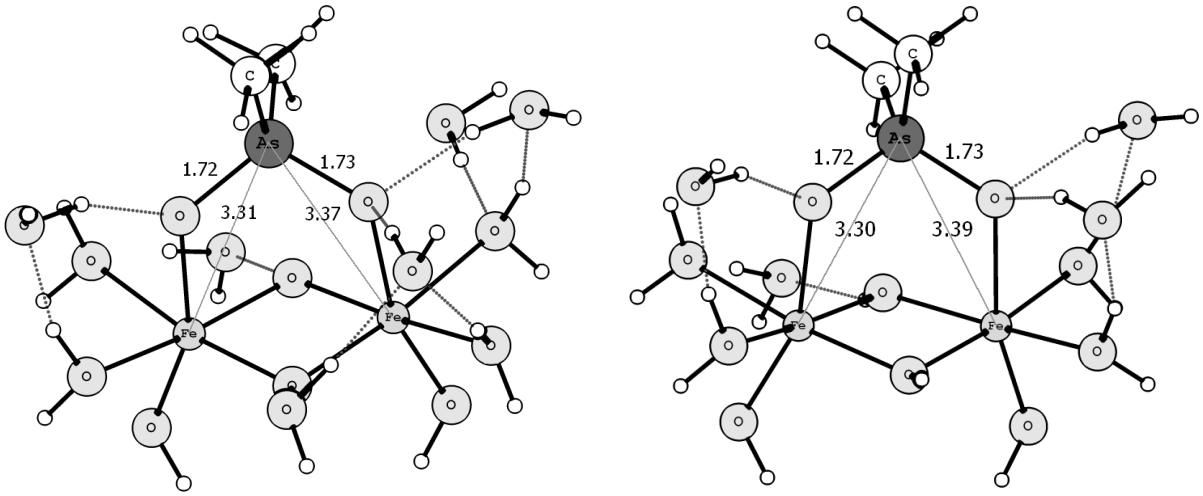

Complex D · $(H_2O)_6$ **Complex D · $(H_2O)_4$**

Figure A3: The effects of adding more explicit waters on the geometry of bidentate Complex D. The differences are minor between 4 and 6 explicit waters with Δd(As-Fe) ranging from 0.01 - 0.02 Å.

Appendix B: Geometries of Complexes A – F calculated using the **SMD** solvation model for the **B3LYP/6-311+G(d,p)** method.

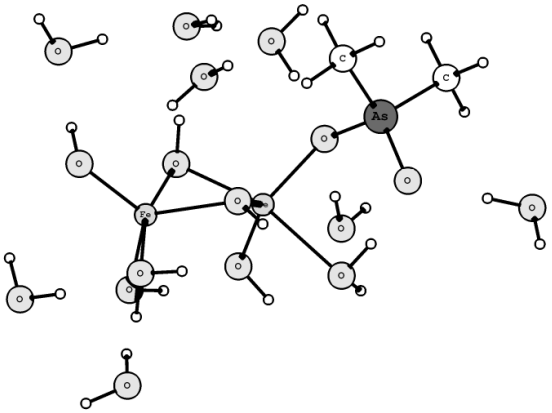

MD Complex A – neutral

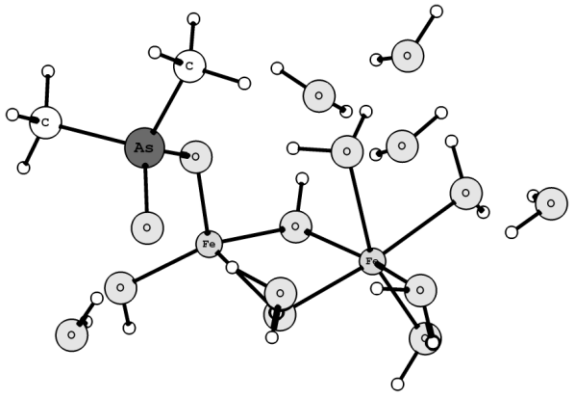

MD Complex B – charge +1

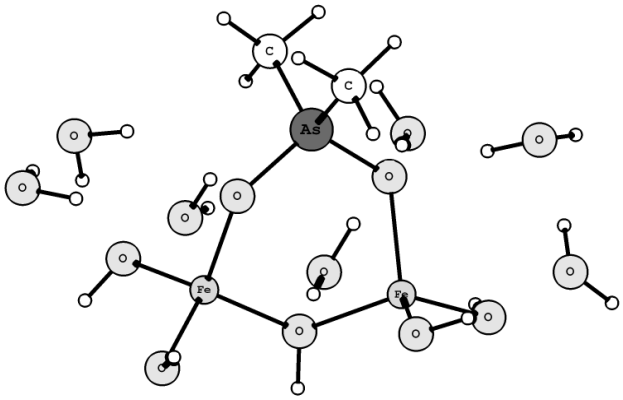

BD Complex C – neutral

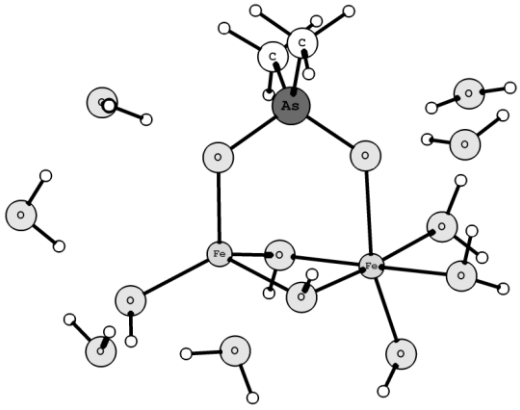

BD Complex D – charge +1

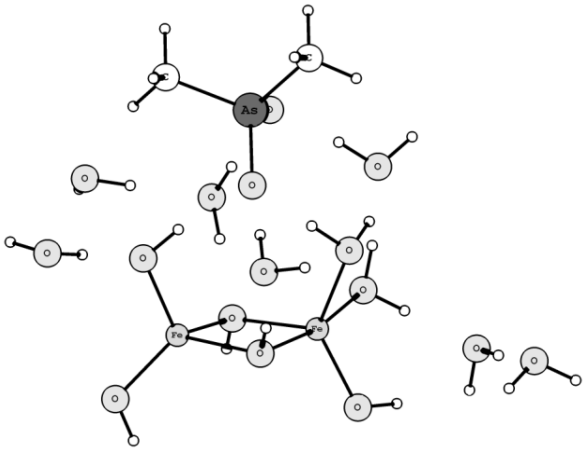

OS Complex E – neutral

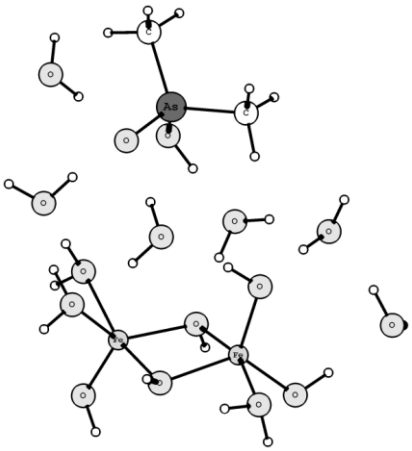

OS Complex F – charge +1

Figure B1: Optimized monodentate, bidentate and outer-sphere complexes A through F calculated using the method B3LYP/6-311+G(d,p) with the SMD solvation model.

Appendix C: Electronic Energies, Thermal Correction to Gibbs free energies and Gibbs energies for **B3LYP/6-311+G(d,p)**, **B3LYP/6-31G(d)** and **BMK/6-311+G(d,p)** with **IEFPCM** solvation model.

Table C1: Electronic Energies, Thermal Corrections and Gibbs energies (in atomic units) calculated with **B3LYP/6-311+G(d,p)** and the **IEFPCM** solvation model.

Molecule	Electronic Energy	Thermal Correction to Gibbs	Gibbs Energy
DMA-H · $(H_2O)_4$	-2772.754455	0.145962	-2772.608493
DMA^- · $(H_2O)_4$	-2772.294358	0.130927	-2772.163432
DMA^- · $(H_2O)_6$	-2925.248388	0.166578	-2925.081810
Iron Hydroxide Surface			
$Fe_2(OH)_6(OH_2)_2$ · $(H_2O)_6$	-3594.564858	0.215210	-3594.349649
$Fe_2(OH)_5(OH_2)_5^+$ · $(H_2O)_4$	-3595.011575	0.228370	-3594.783205
Inner Sphere - Monodentate & Bidentate Clusters			
Complex A - DMA-$Fe_2(OH)_5(OH_2)_3$ · $(H_2O)_5$	-5984.961031	0.275599	-5984.685433
Complex B - [DMA-$Fe_2(OH)_4(OH_2)_5$ · $(H_2O)_4]^+$	-5985.411963	0.288232	-5985.123731
Complex C - DMA-$Fe_2(OH)_5(OH_2)_3$ · $(H_2O)_4$	-5908.479147	0.254553	-5908.224594
Complex D - [DMA-$Fe_2(OH)_4(OH_2)_4$ · $(H_2O)_4]^+$	-5908.933864	0.262624	-5908.671240
Outer Sphere Clusters			
Complex E - DMA ·$(H_2O)_5$ $Fe_2(OH)_5(OH_2)_4$	-6061.432014	0.295201	-6061.136813
Complex F - [DMA-H ·$(H_2O)_4$ $Fe_2(OH)_5(OH_2)_5]^+$	-6061.870896	0.304787	-6061.566109
Complex F2+ - [DMA-H ·$(H_2O)_4$ $Fe_2(OH)_4(OH_2)_6]^{+2}$	-6062.318950	0.319913	-6061.999037
Water Clusters - Leaving groups			
H_2O	-76.46641164	0.003543	-76.462870
OH^- ·$(H_2O)_2$	-228.9303524	0.025412	-228.904940

Table C2: Electronic Energies, Thermal Corrections and Gibbs energies (in atomic units) calculated with **BMK/6-311+G(d,p)** and the **IEFPCM** solvation model.

Molecule	Electronic Energy	Thermal Correction to Gibbs	Gibbs Energy
DMA-H · $(H_2O)_4$	-2771.302979	0.149951	-2771.153028
DMA^- · $(H_2O)_4$	-2770.841646	0.133299	-2770.708347
DMA^- · $(H_2O)_6$	-2923.710780	0.174922	-2923.535857
Iron Hydroxide Surface			
$Fe_2(OH)_6(OH_2)_2$ · $(H_2O)_6$	-3592.850508	0.224463	-3592.626045
$Fe_2(OH)_5(OH_2)_5^+$ · $(H_2O)_4$	-3593.300275	0.233717	-3593.066558
Inner Sphere - Monodentate & Bidentate Clusters			
Complex A - DMA-$Fe_2(OH)_5(OH_2)_3$ · $(H_2O)_5$	-5982.020855	0.284577	-5981.736279
Complex B - [DMA-$Fe_2(OH)_4(OH_2)_5$ · $(H_2O)_4]^+$	-5982.478443	0.304444	-5982.173999
Complex C - DMA-$Fe_2(OH)_5(OH_2)_3$ · $(H_2O)_4$	-5905.589663	0.268908	-5905.320755
Complex D - [DMA-$Fe_2(OH)_4(OH_2)_4$ · $(H_2O)_4]^+$	-5906.044060	0.274134	-5905.769926
Outer Sphere Clusters			
Complex E - DMA ·$(H_2O)_5$ $Fe_2(OH)_5(OH_2)_4$	-6058.446220	0.307043	-6058.139177
Complex F - [DMA-H ·$(H_2O)_4$ $Fe_2(OH)_5(OH_2)_5]^+$	-6058.887406	0.318907	-6058.568499
Water Clusters - Leaving groups			
H_2O	-76.423824	0.004031	-76.419793
OH^- ·$(H_2O)_2$	-228.797545	0.027169	-228.770376

Table C3: Electronic Energies, Thermal Corrections and Gibbs energies (in atomic units) calculated with **BMK/6-311+G(d,p)** and the **IEFPCM** solvation model.

Molecule	Electronic Energy	Thermal Correction to Gibbs	Gibbs Energy B3LYP/6-31G(d)
DMA-H · $(H_2O)_4$	-2770.392726	0.151494	-2770.241232
DMA^- · $(H_2O)_4$	-2769.923454	0.142048	-2769.781406
Iron Hydroxide Surface			
$Fe_2(OH)_6(OH_2)_2$ · $(H_2O)_6$	-3593.834914	0.221807	-3593.613107
$Fe_2(OH)_5(OH_2)_5^+$ · $(H_2O)_4$	-3594.282190	0.230641	-3594.051550
Inner Sphere - Monodentate & Bidentate			
Complex A - DMA-$Fe_2(OH)_5(OH_2)_3$ · $(H_2O)_5$	-5982.098739	0.284235	-5981.814504
Complex B - [DMA-$Fe_2(OH)_4(OH_2)_5$ · $(H_2O)_4]^+$	-5982.558183	0.298828	-5982.259355
Complex C - DMA-$Fe_2(OH)_5(OH_2)_3$ · $(H_2O)_4$	-5905.671304	0.265639	-5905.405665
Complex D - [DMA-$Fe_2(OH)_4(OH_2)_4$ · $(H_2O)_4]^+$	-5906.132157	0.270266	-5905.861890
Outer Sphere Clusters			
Complex E - DMA ·$(H_2O)_5$ $Fe_2(OH)_5(OH_2)_4$	-6058.526915	0.309165	-6058.217750
Complex F - [DMA-H ·$(H_2O)_4$ $Fe_2(OH)_5(OH_2)_5]^+$	-6058.965491	0.313607	-6058.651884
Complex F2+ - [DMA-H ·$(H_2O)_4$ $Fe_2(OH)_4(OH_2)_6]^{+2}$	-6059.429125	0.330758	-6059.098366
Water Clusters - Leaving groups			
H_2O	-76.416296	0.003450	-76.412846
OH^- ·$(H_2O)_2$	-228.763694	0.025761	-228.737933

Appendix D: Uncorrected ν(As-O) frequencies of Structures a, b and Complexes A through F for all four methods used in this study.

Table D1: Uncorrected ν(As-O) frequencies (cm^{-1}) of Structures a, b and Complexes A to F.

Complex	B3LYP 6-31G(d) IEFPCM	B3LYP 6-311+G(d,p) IEFPCM	B3LYP 6-311+G(d,p) SMD	BMK 6-311+G(d,p) IEFPCM
DMA-H · $(H_2O)_4$	727 907 922	668 849	650 809	705 877
DMA^- · $(H_2O)_4$	841 864 869	787 788	747 757 800	823
MD Complex A Charge 0	828 833	754 800	721 779	800 827
MD Complex B Charge +1	801 830 841	740 771 791 815	735 801 816	780 795 828 850
BD Complex C Charge 0	807 853	739 792	741 777	798 832
BD Complex D Charge +1	803 814 837	747 786	737 760	755 813 833
OS Complex E Charge 0	822 839 851	764 773 788 790	746 763 771 783	806 819 854
OS Complex F Charge +1	780 884 887	714 815 838 844	684 787 830	750 862

Appendix E: Example of **calculating Scaling Factors** by minimizing the Sum of the Residuals.

Table E1: Calculated, Corrected and Experimental frequencies (cm^{-1}) and the residuals calculated between corrected and experimental frequencies.

Complexes	Calculated frequencies (T_i) B3LYP/6-311+G(d,p)	Corrected frequencies (T_iF) where F=1.0307	Experimental (E_i) Frequencies DMA/Fe_2O_3 *	Residuals $R_i(F)$
Complex A	757	**780**	775	5.2
	800	**824**	816	8.5
Complex B	740	**763**	775	12.4
	771	**795**	793	1.6
	791	**815**	816	0.8
	815	**840**	840	0.1
Complex C	739	**762**	775	13.4
	792	**816**	816	0.2
Complex D	747	**770**	775	5.1
	786	**810**	816	5.9
Complex E	764	**787**	775	12.4
	773	**797**	793	3.7
	788	**812**	816	3.9
Complex F	714	**736**	735	0.8
	815	**840**	840	0.1
	838	**864**	877	13.4
	844	**870**	877	7.2
			ΣR_i	**94.3**

* From the experimental data found in Reference 3.

Table E2 shows an example of how the Sum of the residuals is minimized when the scaling factor is 1.0307 compared to other scaling factors in that vicinity.

Table E2: Sum of Residuals ΣR_i for different F values.

Scaling factor (F)	Sum of Residuals
1.0285	104.0
1.0295	98.6
1.0300	96.5
1.0307	**94.3**
1.0314	94.9
1.0330	98.2
1.0340	100.5

References

[1] H. Yildirim Erbil. Surface Chemistry of Solid and Liquid Interfaces; Blackwell Publishing Ltd., 2006.

[2] Hartley, W; Lepp, N. W. Remediation of arsenic contaminated soils by iron-oxide application, evaluated in terms of plant productivity, arsenic and phytotoxic metal uptake. Sci. Total Environ. 2008 Feb 1;390(1):35-44.

[3] Adamescu, A.; Mitchell, W.; Hamilton, I.; Al-Abadleh H.A. Insights into the Surface Complexation of Dimethylarsinic Acid on Iron (oxyhydr)Oxides from ATR-FTIR Studies and Quantum Chemical Calculations, Environmental Science and Technology, 2010, 44(20), 7802-7807.

[4] Huang, Y. C. In Arsenic in the environment, part I: Cycling and characterization; Nriagu, J. O., Ed.; Wiley-Interscience: NewYork, 1988.

[5] US EPA, 2008, Chromated Copper Arsenate, http://www.epa.gov/oppad001/reregistration/cca

[6] Christen, K. Chickens, manure and arsenic; Environmental Science and Technology, May 1, 2001.

[7] Cullen, W. R.; Reimer, K. J. Arsenic speciation in the environment. Chem. Rev. 1989, 89, 713–764.

[8] Van Zeghbroeck, B. Principles of Semiconductor Devices, 2007, [online book] http://ecee.colorado.edu/~bart/book/book

[9] Yoon, J.; Jo S.; Chun I.S.; Jung I.; Kim H.S.; Meitl M.; Menard E.; Li X.; Coleman J.J.; Paik U. and J.A. Rogers. GaAs photovoltaics and optoelectronics using releasable multilayer epitaxial assemblies. Nature 465, 329-333 (2010).

[10] US EPA, 2011, Arsenic in Drinking Water, http://water.epa.gov/lawsregs/rulesregs/sdwa/arsenic/index.cfm

[11] World Health Organization. Water-related diseases. Arsenicosis, 2001, [online] Available from http://who.int/water_sanitation_health/diseases/arsenicosis/en/

[12] Wickramasinghe, S. R.; Han, B.; Zimbron, J.; Shen, Z.; Karim, M. N. Arsenic Removal by Coagulation and Filtration: Comparison of Groundwaters from the United States and Bangladesh, Desalination, 169(3), 231-244 (2004).

[13] US EPA, 2011, Arsenic in Drinking Water, http://water.epa.gov/lawsregs/rulesregs/sdwa/arsenic/index.cfm

[14] Cramer, S. P.; Siskin, M.; Brown, L. D.; George, G. N. Characterization of arsenic in oil shale and oil shale derivatives by X-ray absorption spectroscopy. Energy Fuels 2, (1988) 175–180.

[15] Canadian Environmental Protection Act. Priority Substances List Assessment Report. Arsenic and its Compounds. [online] Available from http://www.hc-sc.gc.ca/ewh-semt/pubs/contaminants/psl1-lsp1/arsenic_comp/index-eng.php

[16] Smedley, P.L.; Kinniburgh D.G. A review of the source, behaviour and distribution of arsenic in natural waters. Applied Geochemistry 17 (2002), pp. 517–568.

[17] Brookins, D.G. Eh-pH Diagrams for Geochemistry. 1988. Springer-Verlag, Berlin.

[18] Mandal, B.K.; Suzuki, K.T., Arsenic round the world: a review. Talanta 58 (2002) 201–235.

[19] Hirano, S.; Kobayashi Y.; Cui, X.; Kanno, S.; Hayakawa T.; Shraim, A. The accumulation and toxicity of methylated arsenicals in endothelial cells: important roles of thiol compounds, Toxicol. Appl. Pharmacol. 198 (2004), pp. 458–467.

[20] Kenyon, E.M.; Hughes, M.F. A concise review of the toxicity and carcinogenicity of dimethylarsinic acid. Toxicology 160 (2001) 227–236.

[21] Kubicki, J.D. Interpretation of Vibrational Spectra using Molecular Orbital Theory Calculations, Reviews in Mineralogy and Geochemistry, 42 (2001), pp. 459-483.

[22] Barker, C.M.; Gleeson, D.; Kaltsoyannis, N.; Catlow, C.R.A.; Sankar, G.; Thomas, J.M. On the structure and coordination of the oxygen-donating species in Ti↑MCM-41/TBHP oxidation catalysts: a density functional theory and EXAFS study. Phys. Chem. Chem. Phys., 2002, 4, 1228-1240.

[23] Adamescu, A.; Hamilton, I.; Al-Abadleh, H.A. Thermodynamics of Dimethylarsinic Acid and Arsenate Interactions with Hydrated Iron-(Oxyhydr)oxide Clusters: DFT Calculations, Environmental Science and Technology, 2011, 45, 10438-10444.

[24] PerkinElmer Technical Note. FT- IR Spectroscopy – Attenuated Total Reflectance (ATR) [online]. Available from http://shop.perkinelmer.com/content/TechnicalInfo/TCH_FTIRATR.pdf. 2005.

[25] Sayers, D.E.; Stern, E.A.; Lytle, F.W. New Technique for Investigating Noncrystalline Structures: Fourier Analysis of the Extended X-Ray—Absorption Fine Structure, Phys. Rev. Lett. (1971) 27, 1204–1207.

[26] Shimizu, M.; Arai, Y.; Sparks, D. L. Multiscale assessment of methylarsenic reactivity in soil. 1. Sorption and desorption on soils. Environ. Sci. Technol. 2011, 45, 4293–4299.

[27] Cygan R. T. Molecular Modeling in Mineralogy and Geochemistry, Reviews in Mineralogy and Geochemistry, 42 (2001), pp. 1-35.

[28] Harrison, N.M. An Introduction to Density Functional Theory [online]. Available from http://www.engr.ucsb.edu/~mjgordon/courses/che240a/intro-to-dft.pdf

[29] Ochterski, J.W. Thermochemistry in Gaussian [online]. 2000. Available from http://www.gaussian.com/g_whitepap/thermo.htm

[30] Sherman, D.M.; Randall, S.R. Surface complexation of arsenic(V) to iron(III) (hydr)oxides: Structural mechanism from ab initio molecular geometries and EXAFS spectroscopy. Geochimica et Cosmochimica Acta, (2003) Vol. 67, No. 22, pp. 4223–4230.

[31] Kubicki, J. D.; Kwon, K. D.; Paul, K. W.; Sparks, D. L. Surface complex structures modeled with quantum chemical calculations: carbonate, phosphate, sulphate, arsenate and arsenite, European Journal of Soil Science, 2007, 58, 932-944.

[32] Shared Hierarchical Academic Research Computing Network (SHARCNET). http://www.sharnet.ca.

[33] Becke, A.D. Density-functional thermochemistry. III. The role of exact exchange, J. Chem. Phys., 98 (1993) 5648-52.

[34] Boese, A.D.; Martin, L.M.L. Development of Density Functionals for Thermochemical Kinetics, J. Chem. Phys., 121 (2004) 3405-16.

[35] Foresman, J.B.; Frisch, A. Exploring Chemistry with Electronic Structure Methods. Second Edition. Gaussian, Inc. 1996.

[36] Tomasi, J.; Mennucci, B.; Cammi, R. Quantum mechanical continuum solvation models, Chem. Rev. 2005 August; 105(8)**:** 2999–3093.

[37] Marenich, A.V.; Cramer, C. J.; Truhlar, D.G. Universal solvation model based on solute electron density and a continuum model of the solvent defined by the bulk dielectric constant and atomic surface tensions, J. Phys. Chem. B, 113 (2009) 6378-96.

[38] Orozco, M.; Luque, F.J. Theoretical methods for the description of the solvent effect in biomolecular systems. Chem. Rev. (2000) 100: 4187–4225.

[39] Kubicki, J. D. Self-consistent reaction field calculations of aqueous Al^{3+}, Fe^{3+}, and Si^{4+}: Calculated aqueous-phase deprotonation energies correlated with experimental ln(Ka) and pKa. J. Phys. Chem. A. 2001, 105, 8756–8762.

[40] Shimizu, M.; Arai, Y.; Sparks, D. L. Multiscale assessment of methylarsenic reactivity in soil. 1. Sorption and desorption on soils. Environ. Sci. Technol. 2011, 45, 4293–4299.

[41] Bodner, G.M.; Pardue, H.L. Chemistry (2nd ed.). 1995. New York, John Wiley & Sons, Inc.

[42] Shimizu, M.; Ginder-Vogel, M.; Parikh, S. J.; Sparks, D. L. Molecular scale assessment of methylarsenic sorption on aluminum oxide. Environ. Sci. Technol. 2010, 44, 612–617.

[43] Mitchell, W.; Goldberg, S.; Al-Abadleh, H.A. In-situ ATR-FTIR and surface complexation modeling studies on the adsorption of dimethylarsinic acid and p-arsanlic acid on Iron-(oxyhydr)oxides, Journal of Colloid and Interface Science, 2011, 358(2), 534-540.

[44] Kubicki, J. D.; Kwon, K. D.; Paul K. W.; Sparks D. L. Surface complex structures modeled with quantum chemical calculations: carbonate, phosphate, sulphate, arsenate and arsenite, European Journal of Soil Science, 2007, 58, 932-944.

[45] Shimizu, M.; Arai, Y.; Sparks, D. L. Multiscale assessment of methylarsenic reactivity in soil. 1. Sorption and desorption on soils. Environ. Sci. Technol. 2011, 45, 4293–4299.

[46] IUPAC. “Activation Energy”. Compendium of Chemical Terminology, 2nd ed. (the "Gold Book"). Compiled by A. D. McNaught and A. Wilkinson. Blackwell Scientific Publications, Oxford (1997). XML on-line corrected version: http://goldbook.iupac.org (2006-) created by M. Nic, J. Jirat, B. Kosata; updates compiled by A. Jenkins.

[47] IUPAC. “Transition State Theory”. Compendium of Chemical Terminology, 2nd ed. (the "Gold Book"). Compiled by A. D. McNaught and A. Wilkinson. Blackwell Scientific Publications, Oxford (1997). XML on-line corrected version: http://goldbook.iupac.org (2006-) created by M. Nic, J. Jirat, B. Kosata; updates compiled by A. Jenkins. ISBN 0-9678550-9-8. doi:10.1351/goldbook.

[48] Hammond, G.S. A Correlation of Reaction Rates. J. Am. Chem. Soc., 1955, 77: 334–338.

[49] Merrick, J. P.; Moran, D.; Radom, L. An Evaluation of Harmonic Vibrational Frequency Scale Factors. J. Phys. Chem. A. 2007**,** 111, 11683-11700.